4

Aerodynamic characteristics of wind turbine blade airfoils

W.A. Timmer[1], Christian Bak[2]

[1]DELFT UNIVERSITY OF TECHNOLOGY, DELFT, THE NETHERLANDS; [2]POUL LA COUR TUNNEL, DTU WIND AND ENERGY SYSTEMS, TECHNICAL UNIVERSITY OF DENMARK, LYNGBY, DENMARK

4.1 Introduction

The layout of rotor blades, in terms of twist and chord distribution, depends on the choice of airfoils and consequently, to achieve high performance with acceptable loads, it is important to apply airfoils that are suitable for each specific spanwise part of the blade. Rotor designs until the mid-1980s primarily relied on aviation airfoils, mostly originating from the NACA 4 digit (e.g., NACA 44 series) and 6 digit (e.g., NACA 63 and 64 series) airfoil families (Abbott and von Doenhoff, 1959). The required thickness toward the blade root was generally achieved by linearly scaling up the coordinates of airfoils with smaller thickness. An exception was the FX 77 airfoil series by F. X. Wortmann at Stuttgart University, Germany, in the late 1970s. These airfoils were specifically developed for the Growian, a first-generation 100 m diameter 3 MW turbine, which unfortunately was not very successful. It appeared that the thicker members especially of all these airfoil families suffered from an unacceptable degradation of their performance due to leading edge contamination. Between 1977 and 1984 Wortmann produced a number of airfoils for smaller wind turbines.

The development of a new generation of dedicated wind turbine airfoils started in the mid-1980s with the designs of the S8xx airfoils by Somers and Tangler (Tangler and Somers, 1995). These researchers were followed by Björk (1990), Timmer and van Rooij (2003), Lutz et al. (2004) Fuglsang and Bak (2004) and Bak et al. (2008). Van Dam et al. (2005) and other researchers in the USA presented so-called flatback airfoils for the inner part of the blade, characterized by trailing edge thicknesses of 10% chord or more. In later years more designs appeared, e.g., from a cooperation between DTU Wind Energy (Denmark) and Chong Qing University (China), (Cheng et al., 2014), from ECN (The Netherlands), (Grasso, 2014), from CENER (Spain), (Mendez et al., 2014), from a cooperation between DTU Wind Energy and Vestas (Denmark), (Zahle et al., 2014), from the European project InnWind, (Boorsma, 2015) from ECN/TNO (The Netherlands) together with the University of Strathclyde (UK), (Caboni et al., 2018) and from the Norwegian

Advances in Wind Turbine Blade Design and Materials. https://doi.org/10.1016/B978-0-08-103007-3.00011-2

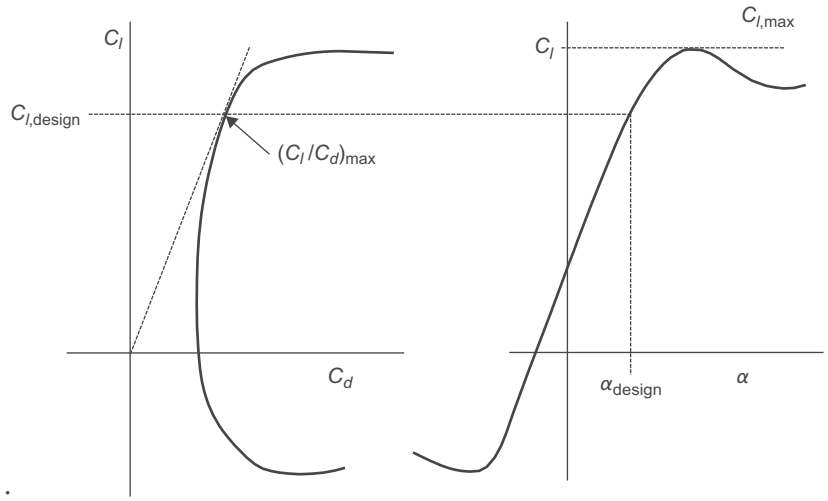

FIGURE 4.1 Key design parameters in the airfoil lift and drag characteristics.

Institute of Science and Technology (Norway), (Hansen, 2018). Each of these designs focussed on different design parameters, such as noise, high Reynolds numbers, thick airfoils, or uncertainties in the input. They are an attempt to further develop and refine the methods for airfoil design. At present, most of the main wind turbine and blade manufacturers develop their own airfoils using optimization techniques. Others use the wind turbine dedicated airfoils designed by the researchers mentioned above, often in combination with the older airfoils from the NACA 63 and 64 6 digit series from the 1930's.

This chapter will focus on airfoils for wind turbine blades and their desired characteristics. The authors assume that the reader has a basic knowledge of aerodynamic concepts such as Reynolds number, pressure distributions, laminar and turbulent boundary layers, boundary layer transition and separation, and airfoil camber and thickness distributions. For an overview of general airfoil aerodynamics the reader is referred to text books, e.g., Anderson (2011).

Fig. 4.1 presents some key design parameters pertinent to airfoil design, which will frequently be addressed in the following sections.

4.2 Computational methods

The design of new airfoils for wind turbine blades requires codes that have the capability to accurately predict the airfoil performance both in the clean and rough surface condition. At present most new airfoils are being designed with panel codes, but with the ever-increasing computational power, CFD codes are rapidly developing as a valuable tool for the design as well. In this chapter, the use of both types of code will be briefly discussed.

4.2.1 Panel codes, XFOIL and RFOIL

For the design and analysis of airfoils, two panel codes are mainly used at present. Somers has used the Eppler code to design the SERI/NREL S8xx-series of airfoils (Tangler and Somers, 1995). However, the most popular code used as a tool for the design of wind turbine airfoils is XFOIL, developed by M. Drela at the Massachusetts Institute of Technology (MIT) (Drela, 1989). XFOIL is a panel code with a strong viscid–inviscid interaction scheme, giving realistic boundary layer properties. The code uses the "e-to-the-nth" method to predict transition. At present XFOIL forms the heart of many optimization codes for airfoil design, since it is fast and relatively easy to use. Moreover, apart from those for the stalled region and the very thick airfoils, XFOIL predictions are generally in fair agreement with measurements.

A derivative of XFOIL, RFOIL, was developed by the Delft University of Technology (TUDelft), the National Aerospace Laboratory (NLR) and the Netherlands Energy Research Foundation (ECN, at present TNO Energy Transition) (van Rooij, 1996). This code features a better convergence around the maximum lift due to the use of different velocity profiles for the turbulent boundary layer and due to modifications in the calculation of the turbulent boundary layer shape factor. This gives an amelioration of the predicted maximum lift coefficient.

In general the prediction of the transition location is good, as demonstrated by Fig. 4.2. The figure shows very good agreement between the XFOIL/RFOIL predicted transition point and the one measured with a stethoscope in the TUDelft low-turbulence wind tunnel up to a few degrees prior to stall.

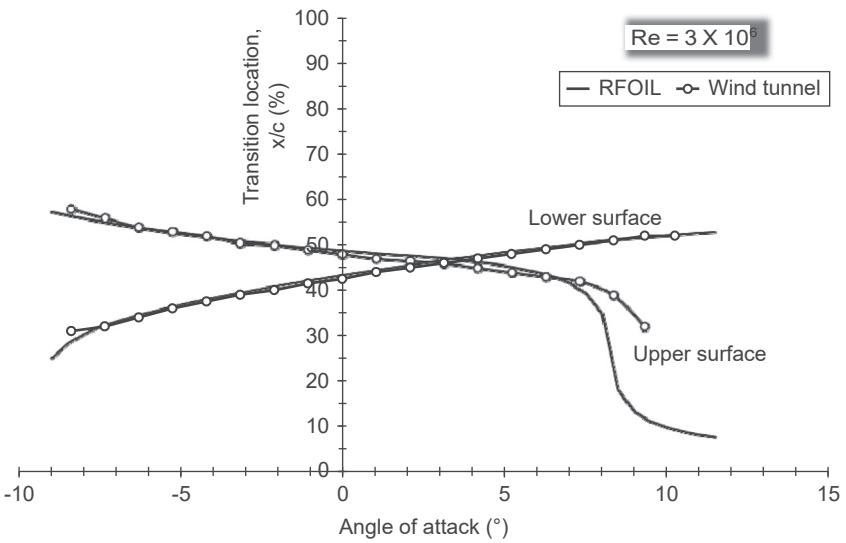

FIGURE 4.2 Comparison of the RFOIL predicted transition location and measurements with a stethoscope in the TUDelft wind tunnel for a 24% thick airfoil.

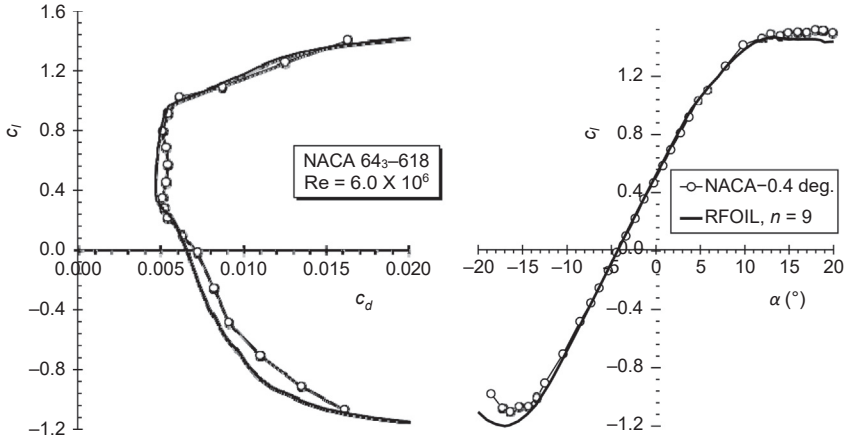

FIGURE 4.3 Comparison of the RFOIL predicted and measured characteristics for airfoil NACA 64_3−618 (Abbott and von Doenhoff, 1959) after modification of the angle of attack by −0.4 degrees due to an assumed model zero-lift misalignment. The amplification factor n had the default value of 9.

In the main, the predicted airfoil performance with free transition is in fair to good agreement with measurements. Fig. 4.3 shows the measured and RFOIL predicted characteristics for airfoil NACA 64_3−618 at a Reynolds number of 6×10^6.

The general trend with XFOIL and RFOIL predictions is that for airfoil relative thicknesses of 18%−21% the drag coefficient is underpredicted by about 8%−10%. For thicker sections this difference increases. The lift curve for Reynolds numbers up to 6×10^6 is predicted quite well. At higher Reynolds numbers RFOIL tends to underpredict the $C_{l,\max}$ (Timmer, 2009).

4.2.2 Computational fluid dynamics

An alternative to panel codes like XFOIL and RFOIL is the use of computational fluid dynamics (CFD), also called Navier−Stokes codes. This type of method solves the nonlinear and, in general, time-varying Navier−Stokes equations numerically. In this section, this method will only be briefly described. For further knowledge about CFD see, e.g., Ferziger (Ferziger and Peric, 2001).

Many different codes exist, both commercial ANSYS Fluent; ANSYS STAR-CD) and research based (Michelsen, 1992, 1994; Sørensen, 1995; OpenFOAM). To use CFD computations to predict the aerodynamic performance of airfoils several steps are needed. Each of these steps is briefly described below.

4.2.2.1 Investigation of airfoil contour

When it is decided to predict the aerodynamic performance of a 2-D airfoil contour the coordinates for this airfoil should be provided in terms of x and y coordinates. Often the coordinates are normalized with the chord length, so that the resulting coordinates are $x/$

c and y/c, with the leading edge in $(x/c, y/c) = (0, 0)$ and the trailing edge in $(x/c, y/c) = (1, 0)$. With these coordinates as the basis the contour should be inspected for smoothness in shape, derivatives, and curvature of the surface. Very small deviations in airfoil shape, introduced by, for example, erroneous splining of the surface, can cause small changes in the pressure distribution around the airfoil. This may lead to premature movement of the location of transition from laminar to turbulent flow toward the leading edge, and may ultimately result in an earlier stall.

4.2.2.2 Mesh generation

Generation of a mesh around the airfoil is necessary to resolve the changes in pressure, velocity, and turbulent entities. In each mesh point, values are stored for the pressure, for the velocities in x and y direction, and for variables describing the turbulent quantities—which could, for example, be the turbulent kinetic energy and the specific dissipation. Several types of meshes can be generated, typically consisting of quadrilaterals or triangles, and referred to as structured or unstructured meshes. In a structured 2-D mesh for an airfoil a typical number of mesh points is 256 along the airfoil surface (starting at the trailing edge and ending at the same point via the leading edge) and 128 normal to the airfoil surface, resulting in 32,768 mesh points. When creating a mesh it is important to resolve the boundary layer in normal direction to the surface, to resolve the flow patterns in the direction of the surface contour and also to resolve the wake behind the airfoil. Specific requirements for the cell sizes in the boundary layer depend on the turbulence model used in the CFD solver.

4.2.2.3 Inspection of mesh

When the mesh has been generated, several geometrical checks have to be carried out. Without giving an exhaustive checklist, it is important to check for

1. orthogonality between the cells, to avoid too much skewness of cells,
2. change of cell size from one cell to its neighbor,
3. height of first cell from airfoil surface, so that the viscous sublayer of the boundary layer at the airfoil is resolved,
4. the aspect ratio of each cell, and
5. the distance from the airfoil to the outer boundary/inlet/outlet, so that the solution is not unintentionally influenced by the boundary conditions, to avoid erroneous solutions. All checks can be automated and will to some extent be based on experience of the degree of deviation that is allowed.

4.2.2.4 Boundary conditions

When setting up the boundary conditions, the flow speed and direction at the inlet and outlet conditions are important. The inlet flow speed, together with the dynamic viscosity, the fluid density and the airfoil chord, determines at which Reynolds number the aerodynamic performance is predicted. Furthermore, the inlet flow direction determines

at which angle of attack the computations are carried out. A constant pressure gradient is typically chosen as the value for an outlet boundary condition.

4.2.2.5 Turbulence model

Wind turbines operate in a Reynolds number regime and in such a way that turbulence is generated at some parts of the airfoil. Therefore, pure laminar computations are insufficient, and either computations assuming fully turbulent flow from the leading edge or computations including the modeling of transition from laminar to turbulent flow are necessary. The turbulence created as a consequence of the boundary layer can be modeled by turbulence models, of which many exist. A commonly used model is the k-ω SST model (Menter, 1994), which works very well for flows with adverse pressure gradients, which is the case for airfoil flow.

4.2.2.6 Computing

Even though CFD has a reputation for being time-consuming, the modern computers of 2022 can obtain a solution for a 2-D airfoil in a few seconds for one angle of attack provided that not too much separation/unsteadiness appears and that a fairly efficient CFD code is used. A polar consisting of, e.g., 20 angles of attack, including angles of attack where separation appears, will take a few minutes. Therefore, computational time is not a critical issue these days, when CFD is used in the evaluation of aerodynamic airfoil performance.

4.2.2.7 Inspection of results

Inspection of results from CFD computations can be carried out at several levels. The first step is to integrate pressure and friction distributions to the airfoil's lift, drag and moment, and analyze these values as a function of angle of attack. These values should be plausible according to the existing knowledge and experience of the user. The second step is to analyze the pressure and friction distributions to reveal unexpected performance. The third and final step is to analyze the flow field in terms of velocity vectors and velocity/pressure/turbulence contours. If all these checks seem to produce plausible values, the solution can be trusted. However, even though a plausible solution to the problem exists, an analysis of the grid resolution should be carried out by increasing the number of cells until the solution (e.g., the lift and drag coefficients) converges monotonically to a unique solution. If the solution is time dependent, a study of time step dependence is also necessary, where the time step is reduced until the solution converges.

4.2.3 Panel codes versus Navier–Stokes codes

In the evaluation of 2-D airfoil performance one can choose between a panel code and a Navier–Stokes code. However, each method has its advantages and drawbacks. A few key issues are listed below.

4.2.3.1 Computational speed

Predicting a lift–drag polar using a panel code takes a matter of seconds, whereas for the CFD code it takes minutes. Thus, the CFD code runs approximately 50 times slower, depending on its computational efficiency. Even though the CFD code is more costly in terms of computational time, this is not necessarily critical or a barrier for using the codes. However, if numerous lift–drag polars are to be predicted, meaning that computational time is a critical factor, consideration should be given to options such as parallel computing.

4.2.3.2 Time for preparation

Comparing preparation time for the two types of codes, the CFD code needs more time than the panel code. Both types of codes need parameter sets, including which airfoil to predict, Reynolds number, and angles of attack. In addition, the CFD code requires generation of a mesh. The amount of extra time needed for this to be done depends on the degree to which the processes are automated. Thus, mesh generation can be very time-consuming if this is being done for the first time, whereas only seconds are needed if the user is experienced and the processes are automated.

4.2.3.3 Computational details

There is much more detail in CFD computations, from which many different kinds of entities can be extracted such as the pressure field, separation patterns, and turbulent kinetic energy. The panel code does not have the same level of capabilities.

4.2.3.4 Comparisons to measurements

Compared with measurements, both the CFD code and the panel code will show good agreement in cases of free transition when flow separation is not dominating the performance characteristics. While panel codes like XFOIL and RFOIL under predict the drag coefficient and show slightly steeper lift gradients, the CFD code tends to over predict the maximum lift coefficient. For Reynolds numbers up to about 6×10^6 RFOIL seems to give fair to good results for the stall region. In this respect Fig. 4.3 is a good example. In the post-stall region, in cases with thick turbulent boundary layers (e.g., resulting from roughness elements) and in situations where significant separation occurs, the CFD code will show better agreement with measurements than the panel code. The same is true for airfoils with a very thick trailing edge such as flatback airfoils.

4.2.3.5 Summary

To summarize advantages and drawbacks for the two methods, the CFD code is superior to the panel code looking at agreement with measurements and computational details. However, both types of codes produce reasonable results, especially for the linear part of the lift curve. Concerning computational speed and preparation time the panel code is superior to the CFD code. Thus, whether a panel code or a CFD code should be chosen

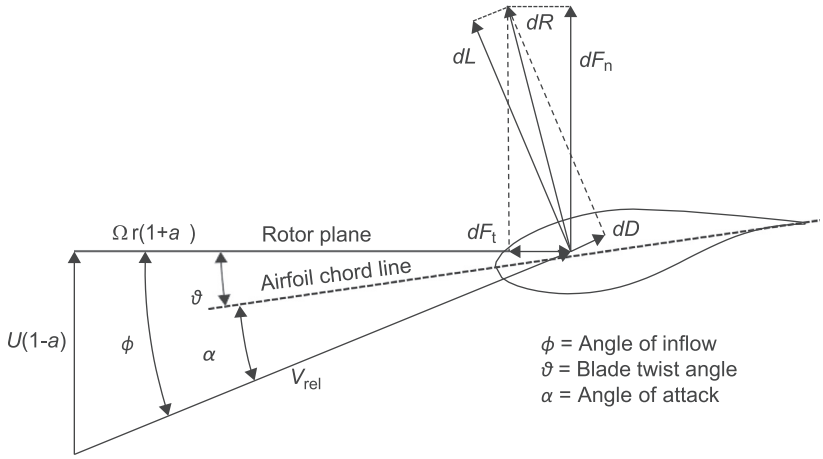

FIGURE 4.4 Velocities and forces diagram on a blade segment.

will depend on the problem that is to be solved, the level of accuracy required, and whether computation time is a factor or not.

4.3 Desired characteristics[1]

Wind turbine dedicated airfoils need distinctive characteristics generally not found in aerospace applications. In a blade, going from the root to the tip, the sections change significantly in maximum thickness and shape. This chapter addresses the required airfoil characteristics for various parts of the blade.

4.3.1 The velocity and forces on a blade element

In Fig. 4.4 the force and velocity vectors on a small spanwise element dr of the blade as a result of the rotational velocity and the wind speed are displayed. The local chord on a radial distance r from the rotor axis is c and the velocity relative to the blade element is V_{rel}.

The lift force on the element is defined as

$$dL = c_l \frac{1}{2}\rho V_{\text{rel}}^2 c dr \tag{4.1}$$

And for the drag force we have

$$dD = c_d \frac{1}{2}\rho V_{\text{rel}}^2 c dr \tag{4.2}$$

Together they form the resultant force dR.

[1]With permission of the van Karman Institute for Fluid Dynamics (VKI). The material in chapters 4.3 and 4.5 has previously been presented in: Timmer and van Bussel (2007).

If we decompose the force dR in a component in the rotor plane and one perpendicular to the rotor plane (dF_t and dF_n, respectively) we find for dF_t:

$$dF_l = d\,L \sin\varphi - d\,D \cos\varphi \tag{4.3}$$

Combining Eqs. (4.1–4.3), and after some rearranging, we find for the torque force:

$$dF_l = \frac{1}{2}\rho V_{\text{rel}}^2 C_l c \left(\sin\varphi - \frac{\cos\varphi}{C_l/C_d}\right) dr \tag{4.4}$$

And for the bending force:

$$dF_n = \frac{1}{2}\rho V_{\text{rel}}^2 c_l c \left(\cos\varphi - \frac{\sin\varphi}{C_l/C_d}\right) dr \tag{4.5}$$

We see that for a given rotational speed and given wind speed both the force that gives the rotor torque, F_t, and the blade bending force F_n are governed by the term $C_l.c$ and the lift–drag ratio of the airfoil C_l/C_d. A high value for the lift–drag ratio of the airfoil is desirable, since it increases the rotor torque and also reduces the bending moments on the blade for a specific lift value.

Designing wind turbine blades involves finding a balance between several sometimes conflicting requirements, as emphasized by the following examples:

- $C_l.c$ needs to be at a certain level to obtain an optimum deceleration of the wind speed. Maximum power will be obtained when the flow is decelerated by approximately 1/3. Thus, high lift coefficients require low chord lengths and vice versa.
- In case of storm loads on a parked rotor, the blade area, and consequently the chord of the blade, should be kept small. Slender blades require high design lift coefficients of the airfoils to keep the term $C_l.c$ at a sufficient level. However, using the same airfoils with slender blades reduces the absolute thickness of the blade sections, which—for sufficient stiffness and strength—may result in more material being required, thus increasing the weight.
- To reduce blade weight, airfoils with a high relative thickness can be used. However, compared to thinner airfoils, thick airfoils have a higher drag. For a small part this comes from a higher friction drag due to the increased wetted surface. Thick airfoils also have higher upper surface velocities. The associated adverse pressure gradients cause additional growth of the boundary layer thickness, resulting in increased pressure drag. In case of leading edge soiling also premature flow separation will occur, which increases the pressure drag even further. Consequently, with respect to high lift–drag ratios over a sufficient range of angles of attack, they cannot compete with thinner airfoils.

Due to strength and stiffness considerations, the maximum airfoil thickness will increase from tip to root. Traditionally wind turbine blades have airfoil relative thicknesses

of about 18% at the tip going to about 25% thickness halfway along the blade span. Airfoil thickness at the root can go up to 40% of the chord, followed by a transition to a cylinder close to the nacelle. However, manufacturers tend to increase this relative thickness for the very big multi-megawatt wind turbine rotors, with a view to decrease blade mass while keeping tip deflection within limits.

According to Eqs. (4.4) and (4.5), for any part of the blade a high lift-to-drag ratio is desired and a choice must be made as to the value of the design lift coefficient, which, for the outer 50% of many modern blades, often lies between 1.1 and 1.25.

4.3.2 Outboard airfoils

For the outboard airfoils of a variable speed pitch-controlled wind turbine, the difference between the $C_{l,\text{design}}$ and the $C_{l,\max}$ must not be too large, to prevent excessive loads in the case of gusts, and not too small, to prevent the rotor from stalling as a result of turbulence in the incoming flow. A difference between the $C_{l,\text{design}}$ and the $C_{l,\max}$ of about 0.4, or in terms of the angle of attack about 5 degrees or more, is considered to be sufficient. In a turbine using stall control, a high $C_{l,\max}$ is advantageous since this leads to smaller chords and to lower storm loads. However, airfoils with a high $C_{l,\max}$ tend to have a more abrupt stall and larger losses in post-stall lift, increasing blade dynamic excitations (see Chapter 5). Furthermore, the associated angle of attack in the case of roughness may be reduced by several degrees, giving large differences in lift at post-stall angles between the contaminated and the clean airfoil. The loss in rated power due to roughness of a fixed pitch turbine is proportional to these differences in lift.

Above rated wind speed, the fixed pitch stall-controlled turbine will have increasingly more separation on the blades, and so, to reduce fatigue loads, the post-stall performance of the blade airfoils must be benign in character. Where this is the case, no sudden large lift-loss due to stalling should occur.

4.3.3 Inboard airfoils

For structural reasons, significant section thickness is required in the root of the blade. Small root chords and restricted blade weight help to overcome problems of transportation of large blades and to keep down structural loads on the shaft and bearings. This calls for airfoils with a high relative thickness, typically 30%–40% chord. The inboard segment of the blade requires a high maximum lift coefficient to deliver sufficient torque at the lower wind speeds. To suppress flow separation and achieve high lift, the inner 50% span of the blades of wind turbines is fitted with vortex generators (VGs) and numerous wind tunnel tests have revealed that VGs can easily boost the maximum lift coefficient to over 1.9.

In a nutshell, desired airfoil characteristics are

- A high lift-to-drag ratio to optimize aerodynamic performance;
- Benign stall characteristics to reduce fatigue loads;

- A high relative thickness to reduce blade weight;
- A high design lift coefficient giving small chords to reduce parking loads;
- Low susceptibility to leading edge contamination.

A flatback airfoil is an airfoil with a very thick trailing edge. The inclusion of a thick trailing edge gives increased lift and decreased sensitivity of the airfoil to blade soiling compared to the base airfoil, thus satisfying the latter two requirements at best. However, the drag is also increased, and unsteadiness in the wake is created due to bluff body vortices. Since the flatback airfoil will be in the inboard region of the blade the net result on the torque of the rotor may—despite the higher drag—be positive. Fig. 4.5 shows a flatback airfoil derived from the DU 97-W-300, see also (Barone and Berg, 2009).

4.4 The impact of leading edge contamination, erosion and Reynolds number

Contamination by insects and leading edge erosion create changes in the characteristics of the airfoils in a blade. Combined with the effect of the increasing Reynolds number with turbine diameter this need to be carefully addressed for a successful blade operation in all conditions.

4.4.1 Effects of roughness

During their lifetime of approximately 20 years, wind turbine blades will suffer some degree of soiling (predominantly from insect collisions, but in offshore machines also from salt crystals) and erosion caused by rain and other weather conditions. This will impact the choice of airfoils.

The disappointing performance of existing aviation airfoils with rough leading edges was the reason that new airfoil designs were introduced in the late 1980s. The potential severity of blade contamination is depicted in Fig. 4.6. It shows the condition of the blade

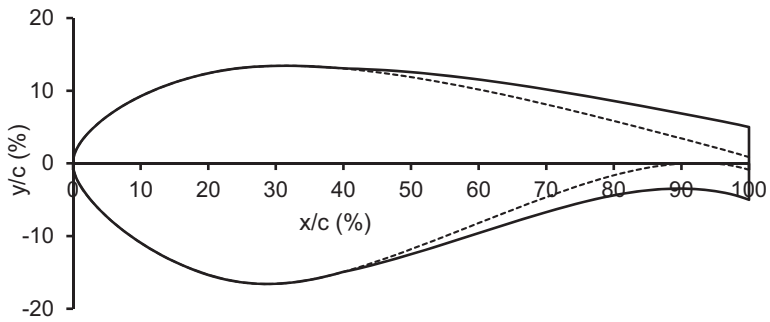

FIGURE 4.5 A flatback airfoil with a trailing edge thickness of 10%, derived from an existing base airfoil (in this case DU 97-W-300) by linearly adding thickness starting at 40% chord (see also Barone and Berg, 2009).

FIGURE 4.6 Contamination by insect debris on the leading edge of a wind turbine blade in Magallón 26 wind farm in Zaragoza, Spain (Blade cleaning.com).

of a turbine in the Magallón 26 wind farm in Zaragoza, Spain, after heavy soiling by insect debris.

Unfortunately, generally it is not known a priori how rough the blade will be and for how long. (In the case illustrated by Fig. 4.6 the insects fly only for a few weeks; however, without cleaning the blades or without rainfall, the roughness will be present for quite some time.) This obscures the direct choice of a set of airfoils, and hence blade design involves some guesstimating of how to incorporate the effect of roughness in the design.

In addition, the roughness on the blade is difficult to replicate during the verification of airfoil performance in the wind tunnel. Basically there are two ways to evaluate the effect of blade soiling in the wind tunnel: the application of wrap-around roughness, as was done during the design and testing campaign for the NACA airfoils, and the use of a tripping device, such as a wire, or a strip of roughness or zigzag tape on both sides of the model. Fig. 4.7 shows the measured effect of grit roughness wrapped around the leading edge of airfoil NACA 64_3−618, the so-called NACA standard roughness (Abbott and von Doenhoff, 1959).

This type of roughness for the 0.61 m chord models consisted of 0.28 mm carborundum grains (no. 60 grit) applied to the airfoil surface at the leading edge over a surface length of $0.08c$ measured from the leading edge on both surfaces. The grains are sparsely spread to cover 5%−10% of this area. Fig. 4.7 shows that the maximum lift−drag ratio is reduced from 170 to 60, a severe reduction of performance indeed.

There is a significant difference between wrap-around roughness and roughness at discrete chord locations (i.e., the NASA standard roughness), as is shown in Fig. 4.8 for the LS(1)-0417 airfoil (McGhee and Beasley, 1973).

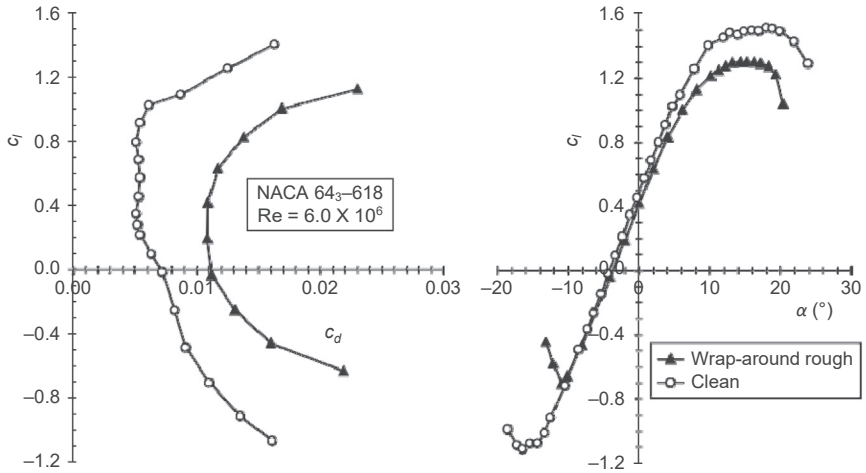

FIGURE 4.7 The effect of NACA standard wrap-around roughness on the performance of airfoil NACA 64_3-618 at a Reynolds number of 6×10^6. Clean airfoil zero-lift angle adjusted by −0.4 degrees for an assumed model misalignment.

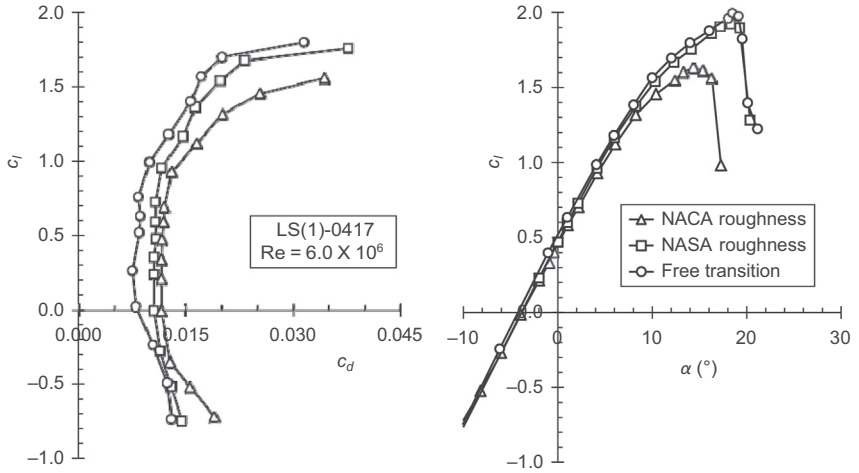

FIGURE 4.8 The effect of NACA standard roughness and NASA standard roughness on the performance of airfoil LS(1)-0417 (McGhee and Beasley, 1973).

NASA standard roughness consisted of 2.5 mm wide strips with no. 80 grit at $x/c = 0.08$ both on the upper and lower surface.

In terms of leading edge contamination the wrap-around roughness condition is mostly treated as a worst-case scenario. The negative impact of leading edge roughness can, however, be greatly surpassed by erosion, caused by rain, hail and other weather conditions. Also erosion comes in stages. Estimates of annual energy production losses for the bigger turbines due to the worst cases of leading edge erosion go up to 5%. An

overview of leading edge erosion of wind turbine blades from the perspective of climate, materials and aerodynamics is made by (Mishnaevsky Jr et al., 2021) where a review of work carried out in this field is described.

4.4.2 The effect of the Reynolds number

The Reynolds number is a scaling parameter and basically gives the ratio of the inertia forces in the flow (associated with velocity, characteristic length and density of the fluid) and the viscous forces (dynamic viscosity). For airfoils it is defined as

$$\mathrm{Re} = \frac{\rho V c}{\mu} \tag{4.6}$$

V is the relative velocity, c is the model chord, ρ is the density of the fluid, and μ is the dynamic viscosity of the fluid. The ratio μ/ρ is called ν, the kinematic viscosity, also depending on the fluid density and temperature. For dry air at standard sea level conditions the value of ν is 14.6×10^{-6}. The higher the Reynolds number, the lesser the viscosity plays a role in the flow around the airfoil.

With increasing Reynolds number the boundary layer gets thinner, which results in a lower drag. Increasing the Reynolds number also has a destabilizing effect on the boundary layer flow, which results in the transition location moving toward the leading edge, leading to a turbulent boundary layer over a longer part of the airfoil surface. The net effect is a lower drag but a smaller low-drag range of angles of attack. This implies that the maximum lift−drag ratio will increase, but that the design lift coefficient will decrease.

This is demonstrated in Fig. 4.9 for airfoil NACA 64_3−418. For a Reynolds number of 3×10^6 the maximum lift−drag ratio is 131 at a lift coefficient of 0.93. At the higher Reynolds number of 9×10^6 the maximum lift−drag ratio has increased to 138 at a reduced lift coefficient of 0.69.

The example demonstrates that for a good design the characteristics at the right Reynolds number should be derived. Since most data are available at a lower Reynolds number, it may be tempting to use these data for the blade design without translation to a higher Reynolds number. This will create uncertainty in the rotor efficiency.

4.5 Noise

From the various noise sources of a wind turbine, trailing edge noise is generally the most dominant one. It finds its origin in the interaction between the turbulent boundary layer and the blade trailing edge and scales with approximately the 5^{th} power of the local velocity, which makes the blade tip area the biggest contributor to wind turbine noise. It is possible to take trailing edge noise into account in the design of outboard airfoils; however, the conditions under which the boundary layer on the blade surface develops change in the course of time under influence of leading edge contamination and erosion.

This makes it rather difficult to define the flow parameters serving as input to the design optimization process.

To reduce trailing edge noise most wind turbine manufacturers add serrated sheet metal plates to the blade trailing edge between 70% to 80% blade span and the tip, sized to the local chord (Figure 4.10). Although in wind tunnel campaigns occasionally reductions of up to 7 dBA are found, field measurements on turbines equipped with serrated trailing edges show reductions up to about 3 dBA.

Due to the fact that the serrated add-ons are an extension of the chord and work as a flap, at moderate flap deflections they can effectively enhance the local section characteristics, giving higher lift while keeping drag and stalling angle approximately constant. This may lead to an increase in turbine power output of over 1 %, depending on the wind speed (Llorente and Ragni, 2020).

While reducing the noise and ameliorating the power performance, the application of serrated trailing edges also results in an increase of blade loading and eventually may adversely impact turbine lifetime. Further research is needed to balance the aerodynamic and structural implications of serrated trailing edges.

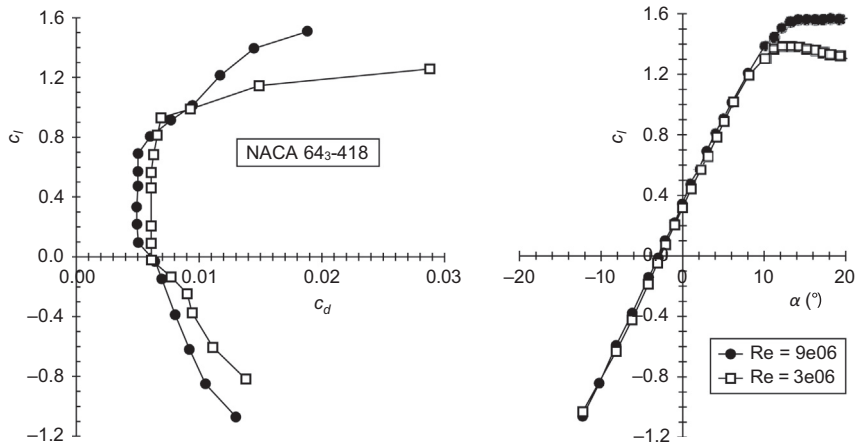

FIGURE 4.9 The aerodynamic performance of airfoil NACA 64_3-418 at Re $= 3 \times 10^6$ and 9×10^6. (Abbott and von Doenhoff, 1959).

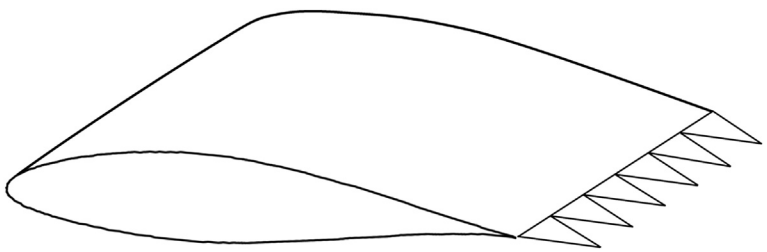

FIGURE 4.10 Triangular serrations added to the trailing edge of an airfoil.

4.6 Airfoil testing

To verify the calculated two-dimensional characteristics of airfoil designs, wind tunnel measurements can be performed. Although this might seem a simple task, in practice it is rather difficult to create the right testing environment to be able to really compare the calculated and measured properties of an airfoil design. Reynolds number, model accuracy, test section velocity, uniformity and turbulence intensity, model blockage, test section longitudinal pressure gradient, test setup, and testing apparatus all have to be accurate to give a good result. These ingredients of a successful test do not stand on their own.

As an example, let us look at the Reynolds number. Eq. (4.6) gives, with μ/ρ replaced by ν,

$$\mathrm{Re} = \frac{V \cdot c}{\nu} \tag{4.7}$$

In atmospheric tunnels, the maximum attainable Reynolds number is set by the maximum test section velocity (max. installed power) and by the maximum allowable model chord (acceptable blockage of the test section at the higher angles of attack). In most wind tunnels the turbulence intensity also goes up while approaching the maximum velocity. The blockage of a test section is expressed in terms of the blockage parameter c/h, with h being the test section height (or width when the model is in the vertical position). Acceptable values of c/h for a test around the maximum lift coefficient are in the order of 0.3−0.35. Modern turbines easily reach Reynolds numbers of 6×10^6 or higher. To get to this Reynolds number, according to Eq. (4.7), we need a model chord of about 1 m with a test section velocity of 90 m/s at standard sea level conditions. The resulting test section dimensions are about 3×2 m, which brings the physical aspect ratio of the model to an acceptable value of 2. For the proper flow quality in terms of velocity uniformity and turbulence intensity a tunnel contraction ratio of at least 9 is desired, giving plenum chamber dimensions of 6×9 m. This already shows the size of the facility. For the combination of a test section area of 6 m^2 and a velocity of 90 m/s an installed power of around 1.5 MW is needed. An example of such a facility is the wind energy dedicated Poul la Cour Tunnel, erected in 2018 at the DTU Risoe Campus headed by DTU Wind Energy. This wind tunnel has a test section size of 3.0m width and 2.0 m height and a contraction ratio of 9. The 2.4MW installed power gives a maximum flow speed of 105m/s. Using a default airfoil chord length of 1.0m, a maximum Reynolds number of 7 million can be obtained under standard sea level conditions, at a turbulence intensity still below 0.1% .It is not difficult to see that, since facilities of this size are not widespread, doing the proper test is often simply a matter of budget.

At 90 m/s test section velocity, in an atmospheric wind tunnel of the size of the Poul La Cour tunnel, Reynolds numbers above 6×10^6 can be obtained by increasing either the velocity or the chord length. Increasing the velocity, however, results in inflow Mach numbers close to 0.3 and may lead to compressibility effects locally on the airfoil.

Increasing the chord length may compromise targets for tunnel blockage and model aspect ratio.

Another way of increasing the Reynolds number is to lower ν in Eq. (4.7). This can either be done in a tunnel with pressurized air (a pressure tunnel) or in a tunnel with an arrangement to lower the temperature of the tunnel gas drastically (a cryogenic tunnel). These are expensive facilities, and in both cases the costs may increase to more than 10 times the cost of a test in an atmospheric tunnel.

Most two-dimensional testing is performed in closed circuit tunnels, although open jet tunnels are being utilized as well. In the latter case a test stand is fully submerged in the jet and the two-dimensionality of the flow is ensured by end plates at both sides of the model. Depending on the correction scheme and the size of the end plates this might give some anomalies in the airfoil's post-stall angle of attack range. Due to the higher power needed for open jet facilities, the achievable Reynolds number is generally much lower compared to closed test section tunnels. In addition, wall interference correction schemes are better defined for closed test sections.

An example of a closed circuit atmospheric tunnel in which many wind turbine airfoils have been tested is the TUDelft low-speed low-turbulence wind tunnel. A schematic of the tunnel layout is given in Fig. 4.11. The tunnel is built in the vertical

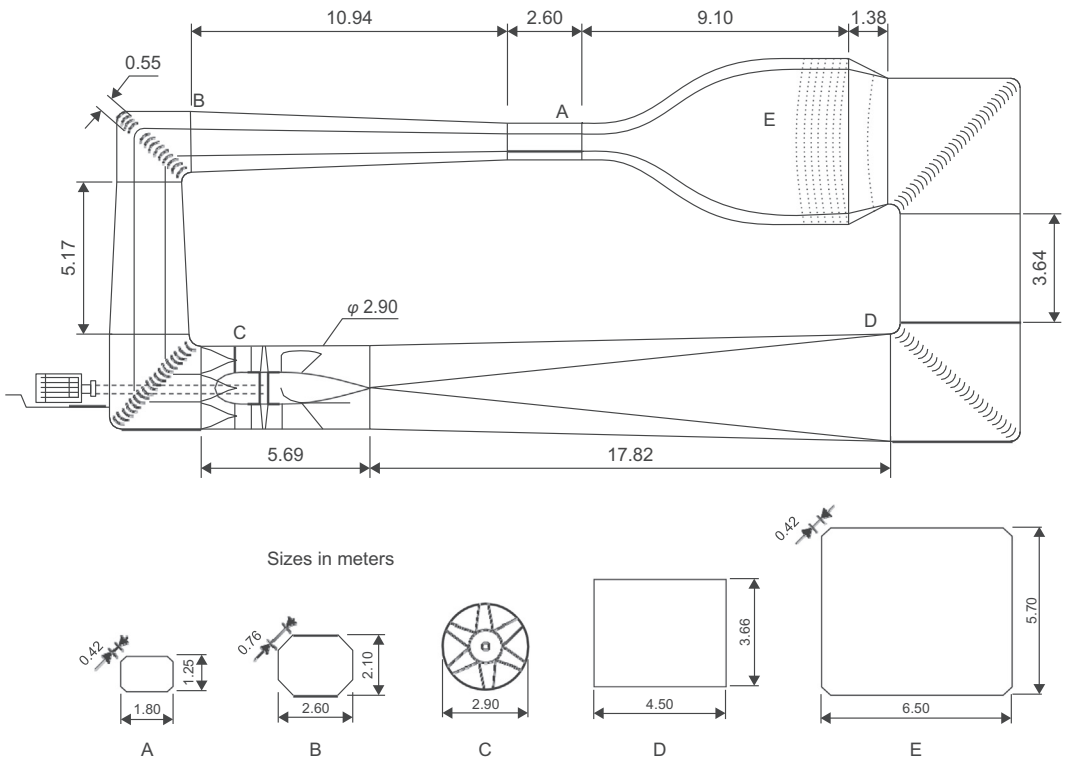

FIGURE 4.11 A schematic of the Delft University low-speed wind tunnel.

plane, and apart from a small part of the contraction and the test section diffuser the entire circuit is of concrete. The installed power is 580 kW. The contraction ratio is 17.8:1, which helps to give the very low-turbulence intensity of 0.02%. The latter is important for the comparison of measurements with calculated characteristics, since increased turbulence adversely affects the boundary layer stability and may lead to early transition.

4.6.1 Setup and testing equipment

Fig. 4.12 shows a model in the TUDelft wind tunnel, looking upstream from behind the model. The model has pressure orifices to measure the surface pressure distribution. At both ends the model is attached to round plates flush with the tunnel walls to set the angle of attack.

In the foreground a wake rake is present at some distance behind the model trailing edge to measure the static and total pressures in the wake, from which the drag coefficient can be derived. The wake rake can move along the span (to check the two-dimensionality of the flow) as well as perpendicular to the model chord (so that it is positioned in the middle of the wake at all angles of attack). The pressures in most wind tunnels are measured with a system consisting of fast electronic pressure transducers with various ranges. Early separation of the model boundary layer at the tunnel wall—model junctions due to interference with the wall boundary layer may influence the flow over the entire model span. Some wind tunnels have a special system to avoid this flow interference either by blowing small air jets in a chord-wise direction at specific chord stations in the comers, or by suction of (part of) the wall boundary layers around the model leading edge.

Forces on a model can be measured if one or both ends of the model are attached to a balance system. If both model ends are not attached to small discs that are flush with (but free from) the tunnel walls then usually a small gap is present between the model

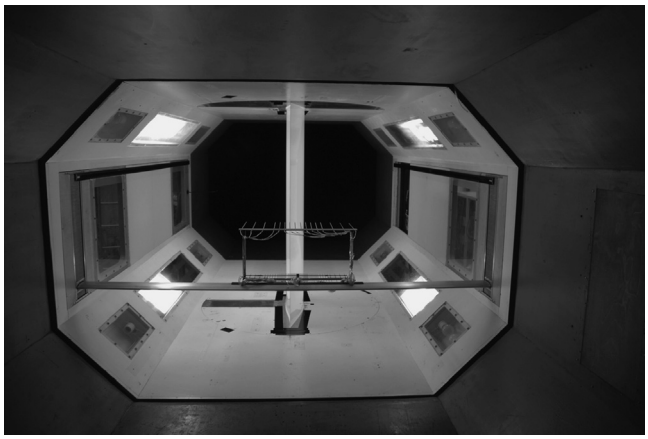

FIGURE 4.12 An upstream view from behind the wake rake on a model with pressure orifices installed in the test section.

and the tunnel walls. In Fig. 4.13 a test setup using the balance system of the Delft tunnel is depicted. To reduce the forces, inserts are present. This is also a way to avoid interference between the relatively thick boundary layer of the tunnel walls and the model boundary layer. The presence of the gaps transforms the model into a high−aspect ratio-wing instead of a two-dimensional model. Depending on the width of the gaps and the aspect ratio of the model the test results need further treatment to remove induced effects on drag and angle of attack. The model is continued between the tables and the walls with separate parts that rotate with the model to ensure a uniform blockage over the entire test section passage.

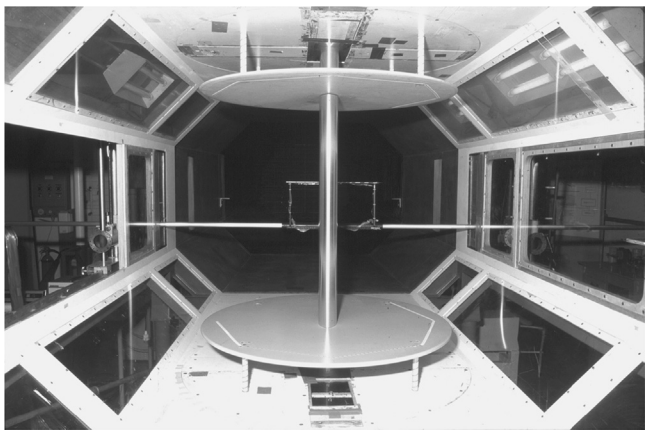

FIGURE 4.13 A test setup using a balance system. Tables are used to avoid interference between boundary layers of the tunnel walls and the model.

4.7 Airfoil characteristics at high angles of attack

When the angle of attack is increased beyond the static stall angle, the suction peak, and consequently the adverse pressure gradient, on the upper surface leading edge grows, while the separation point on the upper surface moves forward. At a specific angle of attack this adverse pressure gradient reaches such a high value that the boundary layer instantly detaches from the leading edge. The airfoil then enters what is called the "deep stall" region, characterized by highly unsteady flow with vortices being shed from the airfoil leading edge with a certain frequency. Due to this periodic flow unsteadiness, the representation of airfoil performance in the deep stall region requires time averaging of the forces and pressures.

Since the value of the suction peak on the leading edge depends on the local thickness distribution, the deep stall angle varies with airfoil leading edge shape. An example is given in Fig. 4.14. Fig. 4.15 shows the associated pressure distributions for airfoil DU 96-

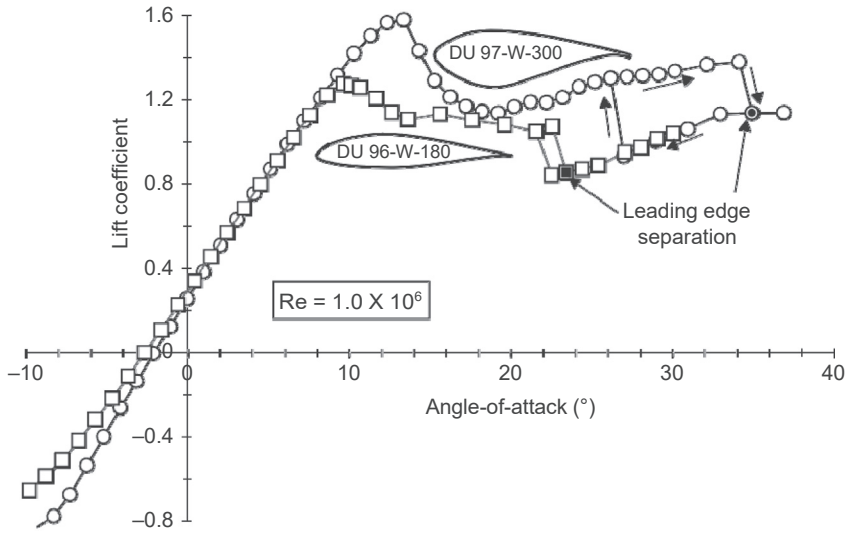

FIGURE 4.14 The measured lift curve for an 18% and a 30% thick wind turbine airfoil at a Reynolds number of 1.0×10^6, showing the deep stall angle (Timmer, 2010).

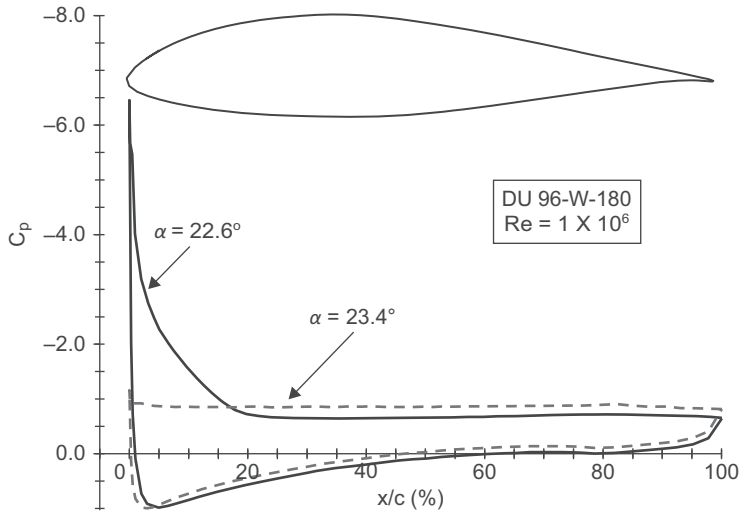

FIGURE 4.15 Measured pressure distributions for airfoil DU 96-W-180 at the boundary of the deep stall region (Timmer, 2010).

W-180 just before and in deep stall. Timmer (Timmer, 2010) derived a relation between the leading edge shape and the deep stall angle by correlating the measurements on a number of airfoils in the TUDelft low-speed low-turbulence wind tunnel: the deep stall angle is equal to 1114 times the airfoil *y/c* ordinate at the x/c=0.0125 station. The relation is graphically presented in Fig. 4.16. It must be noted that the separation here is the

result of laminar bubble bursting which makes the onset of deep stall vary with Reynolds number, turbulence intensity and general flow conditions on the leading edge (e.g., contamination). Fig. 4.16 was constructed using wind tunnel tests in low-turbulence intensity flow for clean models at a Reynolds number of 1×10^6. The deep stall angle may be notably different in other flow conditions.

During starts and stops of a rotor and under parked conditions the blades see very high angles of attack and for the purpose of loads calculations it is necessary to establish the performance of the blade in these conditions. Generally this starts with an evaluation of the quasi-steady two-dimensional characteristics of the airfoils incorporated in the blade. Fig. 4.17 gives an example of the characteristics at high angles of attack for two wind turbine airfoils measured in a wind tunnel.

Since these measurements have not been performed for all wind turbine airfoils, and the deep stall characteristics cannot be derived without using lengthy CFD calculations, a number of methods for modeling the lift and drag curves on the basis of existing information have been presented.

Viterna and Corrigan (1981) proposed an empirical model following from derivation of the post-stall airfoil performance, assuming constant rated power for three rotor configurations, of a 100 kW and a 200 kW stall-controlled wind turbine, using strip theory. The method is widely used and returns values for the lift and drag coefficient at high angles of attack starting from the stall point of the airfoil lift curve.

The equations are partly based on the variation of the maximum flat plate drag coefficient with aspect ratio as proposed by Hoerner (Hoerner, 1965), given in Eq. (4.8):

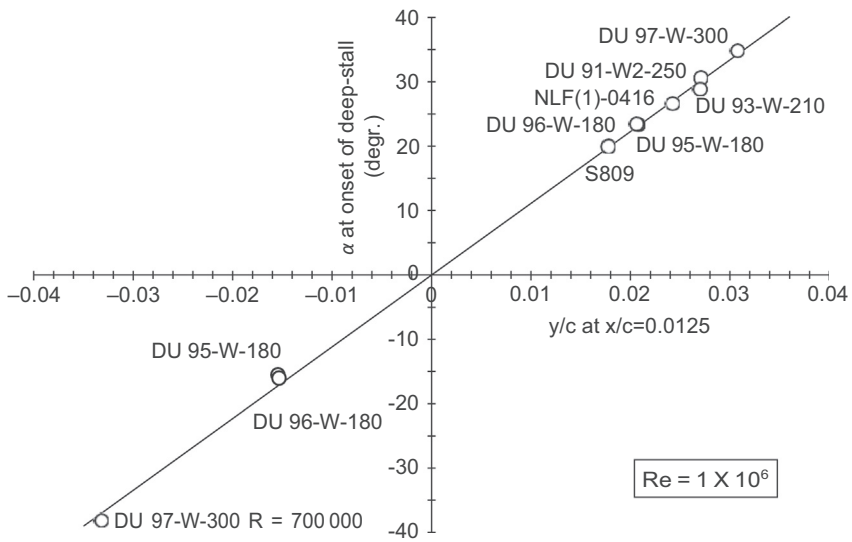

FIGURE 4.16 Variation of deep stall angle with upper surface leading edge thickness for a number of wind turbine airfoils (Timmer, 2010).

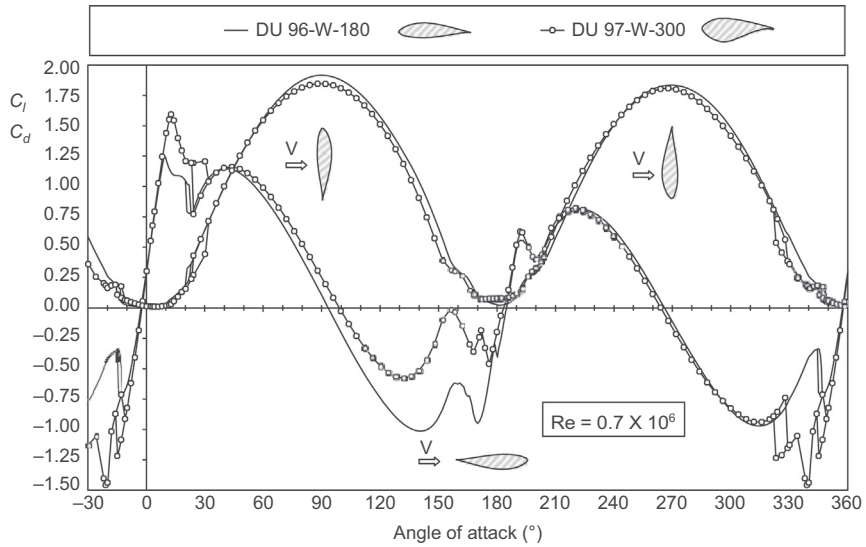

FIGURE 4.17 The measured aerodynamic performance of two airfoils at high angles of attack (Timmer, 2010).

$$C_{D,\max} = 1.111 + 0.018\,AR \quad \text{for} \quad AR < 50 \tag{4.8}$$

$$C_{D,\max} = 2.01 \quad \text{for} \quad AR \geq 50$$

Here the aspect ratio is defined as the blade radius divided by the chord length at 75% of the span: $AR\ R\ c_{0.5R}$.

The lift and drag coefficients follow from

$$C_D = C_{D,\max} \sin^2 \alpha + K_1 \cos \alpha \tag{4.9}$$

with

$$K_1 = \frac{C_{D,s} - C_{D,\max} \sin^2 \alpha_s}{\cos \alpha_s} \tag{4.10}$$

and

$$C_L = \frac{1}{2} C_{D,\max} \sin^2 \alpha + K_2 \frac{\cos^2 \alpha}{\sin \alpha} \tag{4.11}$$

where

$$K_2 = (C_{L,s} - C_{D,\max} \sin \alpha_s \cos \alpha_s) \frac{\sin \alpha}{\cos^2 \alpha} \tag{4.12}$$

The index s in these equations indicates the point of maximum lift in the airfoil lift curve, matching the pre-stall characteristics with the calculated post-stall performance of the airfoil.

Despite the fact that the use of the method is widespread and seems to have worked for the two machines under investigation, one should realize that the method actually

does not return two-dimensional force coefficients, but is a global one; i.e., the equations are based on matching the total maximum power of the rotor, which means that all (three-dimensional) effects are included. This specifically covers the rotational effects that are dominant at the inboard part of the blade. As the next chapter will show, these effects are dependent on the local value of the rotor solidity, c/r, which makes them also dependent on the blade layout.

Additionally, the authors mention that they have switched off the (Prandtl−Glauert) tip-loss correction in their blade element momentum (BEM) calculations, as they have already accounted for the aspect ratio of the blade in Eq. (4.8). However, the tip-loss correction in BEM theory is not a correction for the *noninfinity of the blade*, but rather a correction for the fact that instead of an actuator disc a *finite number of blades* is used to extract the power, which has an entirely different physical meaning.

Tangler and Kocurek (2005) investigated the resulting predicted power for the NREL 10 m diameter Unsteady Aerodynamics Experiment turbine using different input parameters in the Viterna and Corrigan method. They concluded that good results were obtained when the matching point is the deep stall angle of the airfoil instead of the angle for maximum lift.

Lindenburg (2003) and Spera (2010) each present their own set of equations, partly based on the two-dimensional drag coefficient at 90 degrees angle of attack, $C_{d,\max}$, and also including the effect of aspect ratio. Lindenburg constructed a relation for $C_{d,\max}$, using the leading edge radius in combination with the airfoil trailing edge angle. His analysis mainly includes NACA 4-digit airfoils and other shapes found in the literature, such as ellipses, cylinders, and wedges. Spera uses the same collection of airfoil maximum drag coefficients and adds the drag coefficient at the onset of deep stall to construct his drag curve. The majority of the $C_{d,\max}$ data being used by Lindenburg and consequently also by Spera have a value higher than the widely used flat plate maximum drag coefficient of 1.98. Also, Eq. (4.8) points at a flat plate maximum drag value for all airfoils. This seems a bit strange. Airfoils have one rounded and one sharp end and a trailing edge angle in the main falling in the range of +10 to −10 degrees. One would expect a value of the maximum drag coefficient below 2. Timmer (2010) suggested a simple relation between $C_{d,\max}$ and the y/c ordinate at x/c=0.0125, following the work of Gault (Gault, 1957), who used this parameter to typify airfoil stall. Gault and later Bak et al (Bak et al., 1999) investigated the type of stall and observed a correlation between the shape of the airfoil leading edge and the tendency to thin airfoil stall, leading edge stall, trailing edge stall and combined leading edge stall and trailing edge stall. The analysis of Bak et al. indicated a correlation between the slope of the airfoil surface at x/c=0.02 and the stall type, comprising more airfoils than Gault's parameter.

$$C_{d,\max} = 1.976 - 5.366\left(\frac{y}{c}\right)_{x/c=0.0125} + F_{TE} * \varsigma F_{TE} = -0.00246 - 0.05815\left(\frac{y}{c}\right)_{x/c=0.0125} \tag{4.13}$$

This $C_{d,\max}$ relation was later (Timmer, 2020) subdivided into a contribution due to the leading edge shape and one due to the trailing edge angle ζ. Eq. (4.13). The trailing edge angle is defined positive when it points in flow direction. The equation shows that the highest C_d is achieved by having two sharp edges (flat plate, y/c=0) and that the $C_{d,\max}$ reduces with increasing leading edge thickness. According to Eq. (4.13) a typical 25% thick mid-span airfoil like the DU 91-W2−250 ($y/c = 0.031$) and a lower surface trailing edge angle of -10.23° would have a $C_{d,\max}$ at 90 degrees of 1.853. The Reynolds number of the data was in the order of 0.5×10^6 to 0.75×10^6. With increasing Reynolds number the airfoil base pressure decreases, which increases the drag and puts the predicted $C_{d,\max}$ values at the lower end of what can be expected. Using Eq. (4.13) the maximum drag coefficients at positive and negative angles of 10 airfoils is predicted within 2.3%.

Due to the unsteady nature of the flow at high angles of attack, there is a great deal of uncertainty in the performance of airfoils and consequently also in the performance of blades, where, in addition, the aspect ratio has an important contribution. The frequency of the vortex shedding, characterized by the Strouhal number, might affect the aeroelastic behavior of the wind turbine.

In view of this unsteadiness and its consequences for the blade aeroelastic behavior, the modeling of wind turbines in standstill has been extensively investigated and discussed (Skrzypiński, 2012; Johansen et al., 2004). The 3-D CFD computations in (Johansen et al., 2004) show blade section $C_{d,\max}$ values of 1.3 (already known from experience) to 1.5 toward the tip of the blade, leading to a mean blade $C_{D,\max}$ of around 1.3.

Despite the development of these models describing high angle of attack aerodynamics, the level of uncertainties that remain justifies more research on this subject.

4.8 Correction for centrifugal and Coriolis forces

To predict the performance of wind turbines, calculations of power and loads are carried out using aeroelastic codes, where the rotor aerodynamics essentially are modeled by the BEM theory, because this model is fast and robust. Using this model the operational conditions, the blade geometry, and the airfoil characteristics are required to describe the forces on the blade in terms of lift and drag coefficients as a function of angle of attack. Airfoil characteristics used in BEM calculations are typically based on 2-D wind tunnel tests on airfoils as described previously in this chapter. However, a direct application of the 2-D characteristics shows poor agreement between measured and calculated loads and power especially for rotors with significant flow separation. Therefore, there is a need for correction of the airfoil characteristics to include centrifugal and Coriolis effects that occur for separated flows. In the following sections, several existing correction models are described. If pitch regulated variable speed (PRVS) wind turbines are considered, the centrifugal and Coriolis effects will not be as significant as for the stall regulated wind turbines, because a significant part of a PRVS rotor operates in attached flow for most of the time. However, all rotors will experience separated flow

to some extent during operation and therefore correction for centrifugal and Coriolis forces is necessary.

4.8.1 Existing 3-D correction models

The need to correct for centrifugal and Coriolis forces, which combined effect in the following will be called "3-D correction" of airfoil characteristics, has resulted in several models in which the lift coefficient, and for some models also the drag coefficient and even the moment coefficient, are corrected in the case of flow separation from the airfoil sections. Models have been developed by Snel et al. (1993), Du and Selig (1998), Chaviaropoulos and Hansen (2000), Lindenburg (2004), and Bak et al. (2006). Using these models, 2-D airfoil characteristics are corrected with a limited input. The first four models are expressed as shown in Eq. (4.14):

$$\begin{aligned} c_{l,3D} &= c_{l,2D} + f\left(\frac{c}{r}, \ldots\right)\Delta c_l \\ c_{d,3D} &= c_{d,2D} + f\left(\frac{c}{r}, \ldots\right)\Delta c_d \end{aligned} \tag{4.14}$$

where 2-D refers to the two-dimensional characteristics of the airfoil established from calculations or wind tunnel measurements and c/r is the ratio between the local chord length and the radius at a certain blade span-wise position (local blade solidity). The expression $f(c/r, \ldots)$ means that all models are a function of c/r, but that they also can be a function of other parameters. Δc_l and Δc_d denote the difference between the c_l and c_d that would exist if the flow did not separate. The terms c_l and c_d are the measured or computed lift and drag coefficients including separation. The function $f(c/r, \ldots)$ varies from model to model and can shortly be described as follows:

Snel et al.:

$$f_{c_l} = 3\left(\frac{c}{r}\right)^2 \tag{4.15}$$

Lindenburg:

$$f_{c_l} = 3.1\left(\frac{\omega r}{V_{\text{rel}}}\right)^2\left(\frac{c}{r}\right)^2 \tag{4.16}$$

Du and Selig:

$$f_{c_l} = \frac{1}{2\pi}\left[\frac{1.6(c/r)}{0.1267}\,\frac{a-(c/r)^{\frac{d}{\Lambda}\frac{R}{r}}}{b+(c/r)^{\frac{d}{\Lambda}\frac{R}{r}}} - 1\right] \tag{4.17}$$

$$f_{c_d} = \frac{1}{2\pi}\left[\frac{1.6(c/r)}{0.1267}\,\frac{a-(c/r)^{\frac{d}{2\Lambda}\frac{R}{r}}}{b+(c/r)^{\frac{d}{2\Lambda}\frac{R}{r}}} - 1\right]$$

$$\Lambda = \frac{\omega R}{\sqrt{U_{\text{vinal}}^2 + (\omega r)^2}}$$

where $a = b = d = 1$.

Chaviaropoulos and Hansen:

$$f_{C_l,C_d} = a\left(\frac{c}{r}\right)^h \cos^n(\theta), \tag{4.18}$$

where a = 2.2, h = 1 and n = 4

The models by Snel et al. and Lindenburg solely contain a correction for c_l and not for c_d. Furthermore, Lindenburg has also proposed a model based on c_n, which is the force coefficient normal to the chord direction.

The model by Bak et al. is somewhat different from the above-described methods because it models the differences between 3-D and 2-D on the level of the pressure distributions and not on the level of the force coefficients. The model consists of four steps. First the difference in pressure distribution along the chord at a certain radial station is predicted as shown in Eq. (4.19):

$$\begin{aligned}\Delta Cp &= \frac{5}{2}\left(1-\frac{x}{c}\right)^2\left(\frac{\alpha-\alpha_{f=1}}{\alpha_{f=0}-\alpha_{f=1}}\right)^2\sqrt{1+\left(\frac{R}{r}\right)^2}\;\frac{(c/r)}{1+\tan^2(\alpha+\theta)}\\ \max(\Delta Cp) &= \frac{5}{2}\sqrt{1+\left(\frac{R}{r}\right)^2}\;\frac{(c/r)}{1+\tan^2(\alpha+\theta)}\end{aligned} \tag{4.19}$$

Then the differences between 3-D and 2-D in normal and tangential force coefficients and the moment coefficients are computed as shown in Eq. (4.20):

$$\begin{aligned}\Delta c_x &= \int_{x/c=0}^{x/c=1}\Delta Cpd\left(\frac{x}{c}\right)\\ \Delta c_t &= \int_{y/c=y/c(\text{leading\_edge})}^{y/c=y/c(\text{trailing\_edge})}\Delta Cpd\left(\frac{x}{c}\right)\\ \Delta c_m &= -\int_{x/c=0}^{x/c=1}\Delta Cp\left(\frac{x}{c}-0.25\right)\mathrm{d}\left(\frac{x}{c}\right)-\int_{y/c=y/c(\text{leading\_edge})}^{y/c=y/c(\text{trailing\_edge})}\Delta Cp\left(\frac{y}{c}\right)\mathrm{d}\left(\frac{y}{c}\right)\end{aligned} \tag{4.20}$$

where Δc_n, Δc_t, and Δc_m are additional contributions to the 2-D coefficients.

Then the normal and tangential force coefficients and the moment coefficients are computed according to Eq. (4.21):

$$\begin{aligned}c_{n,3D} &= c_{n,2D} + \Delta c_n\\ c_{t,3D} &= c_{t,2D} + \Delta c_t\\ c_{m,3D} &= c_{m,2D} + \Delta c_m\end{aligned} \tag{4.21}$$

where $c_{n,3D}$, $c_{t,3D}$, and $c_{m,3D}$ are the 3-D corrected coefficients.

Finally, the lift and drag coefficients are derived according to Eq. (4.22):

$$\begin{aligned}c_{l,3D} &= c_{n,3D}\cos(\alpha) + c_{t,3D}\sin(\alpha)\\ c_{d,3D} &= c_{n,3D}\sin(\alpha) - c_{t,3D}\cos(\alpha)\end{aligned} \tag{4.22}$$

4.8.2 An example of the application of 3-D models to a wind turbine rotor with stall control

In this example some of the 3-D correction models are applied to the NREL 10 m diameter stall regulated rotor tested in the NASA Ames 24 × 36 m wind tunnel (Hand et al., 2001). The predictions of overall rotor power and thrust and local blade airfoil characteristics are compared to measurements. These comparisons illustrate not only strengths and weaknesses of the different models but also the capability of correction methods in general. Key parameters for the rotor are shown in Table 4.1.

Before a 3-D correction is carried out, it is important to review the 2-D airfoil data. In this process it should be ensured that (1) there is correspondence between the Reynolds number in the wind tunnel test/computations and in the rotor operation and (2) maximum lift and maximum lift−drag ratio are not too optimistic, because the airfoil surface as measured in the wind tunnel could be very smooth and clean and therefore not representative of a typical wind turbine blade surface. When trustworthy 2-D airfoil data is established, a 3-D correction can be carried out. In Figs. 4.18 and 4.19 the airfoil characteristics for the rotor at two radial sections are presented. In addition to 2-D wind tunnel data, and the data extracted from the NREL/NASA Ames test, four 3-D correction models are also shown: Snel et al. (1993), Chaviaropoulos and Hansen (2000), Lindenburg (2004) and Bak et al. (2006) It can be seen that the models by Snel et al. and Bak et al. predict the airfoil characteristics quite well at the inner section at radius 30%. However, it should be noted that the model by Snel et al. does not include a 3-D correction for the drag. Furthermore, the model by Bak et al. is the only model in Fig. 4.19, where c_l shows a negative slope for angles of attack above 25−30 degrees, something which has been observed in several measurement campaigns (Madsen and Rasmussen, 1988; Bak, 2004; Bak et al., 2006).

In Fig. 4.20 the mechanical power and the thrust are depicted. It shows that the models by Chaviaropoulos and Hansen overpredict and the model by Lindenburg underpredicts both power and thrust. However, the models by Snel et al. and Bak et al. predict both the power and thrust fairly well. At wind speeds above 13 m/s all models show a significant drop in power.

Table 4.1 Data for the NREL/NASA Ames rotor.

Number of blades	2
Rotor diameter (m)	10.058
Rotational speed (RPM)	72.0
Design tip−speed ratio, Λ (−)	6.3
Tip speed (m/s)	37.9
Airfoil series	S809
Power control	Stall

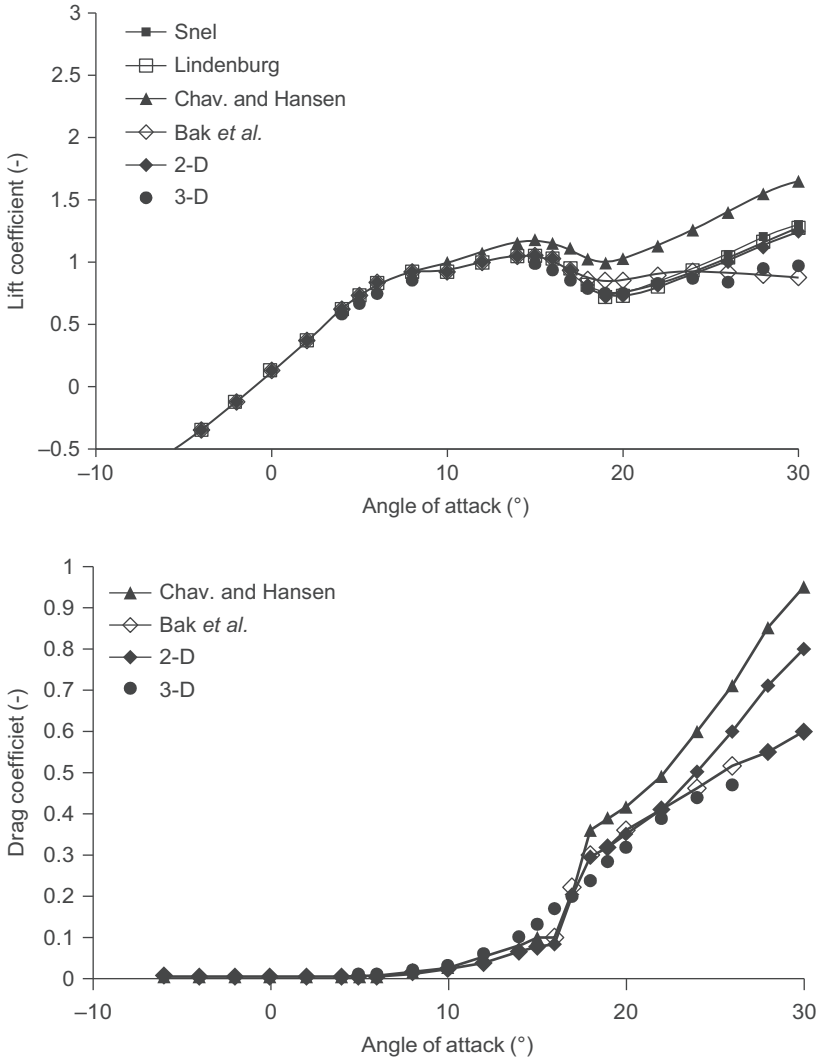

FIGURE 4.18 3-D corrected airfoil lift (top) and drag (bottom) characteristics for $r/R = 80\%$ compared to 2-D measurements and measured 3-D data.

The conclusion from this example is that the predicted power and loads agree better with measurements when the airfoil characteristics are corrected for 3-D using the existing models. However, even though a fair agreement in power and loads is reached, there are still shortcomings in the 3-D correction models. These are related to both the ability of the tools to predict the onset of stall in 2-D and the understanding of the impact of centrifugal and Coriolis forces on the separated flow.

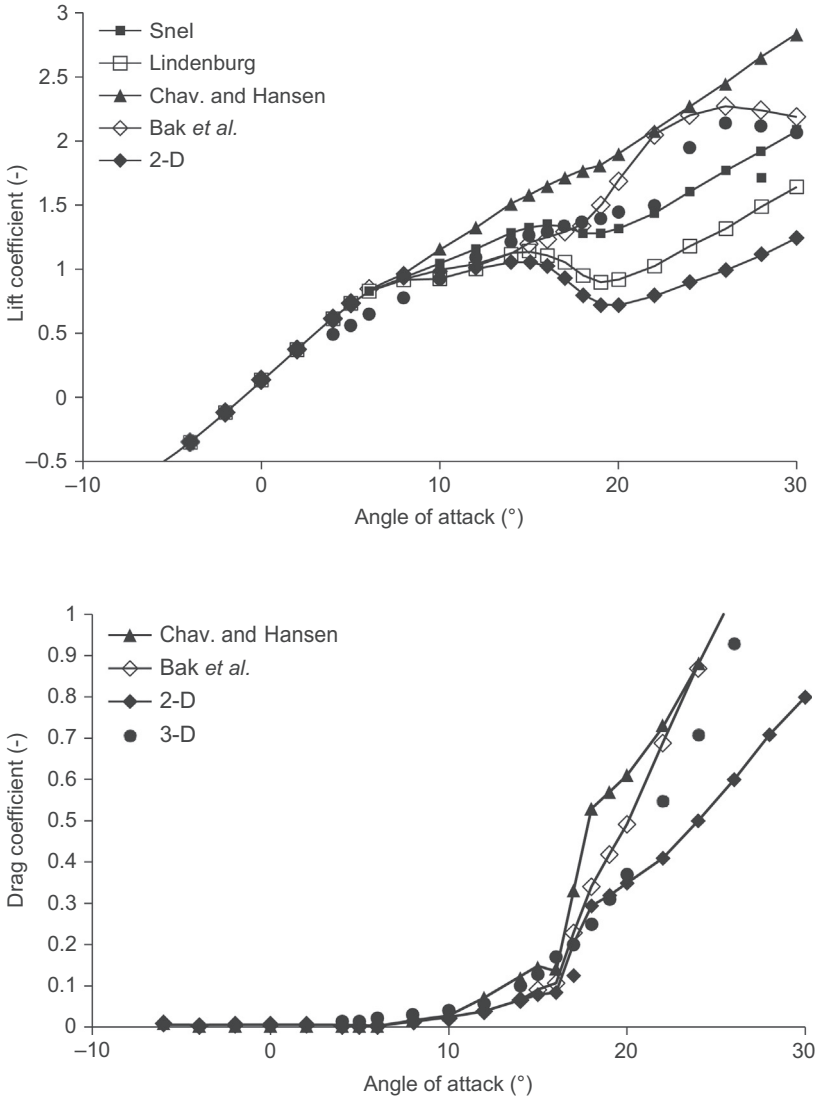

FIGURE 4.19 3-D corrected airfoil lift (top) and drag (bottom) characteristics for $r/R = 30\%$ compared to 2-D measurements and measured 3-D data.

4.9 Establishing data for blade design

The first step in aerodynamic blade design is to find suitable airfoils and their characteristics. Even at this point, choices need to be made regarding the value of the design lift coefficient and associated lift−drag ratio in relation to the maximum relative thickness of the section in the light of the required strength and stiffness of the blade. Based on the

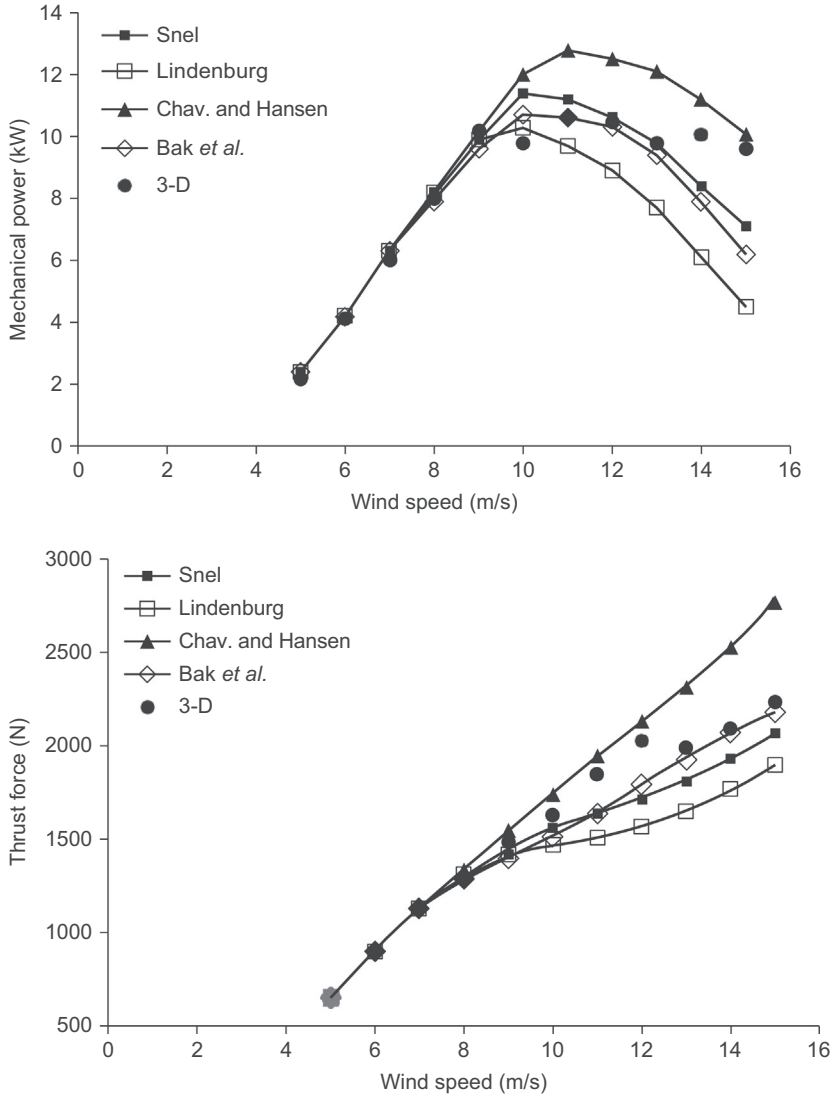

FIGURE 4.20 Measured 3-D data and computed mechanical power and thrust force for the NREL rotor.

in-plane force dF_t referred to previously in this chapter, the torque of the rotor follows from

$$Q = \int_0^R B\,\frac{1}{2}\,\rho V_{rel}^2 C_l c\left(\sin\varphi - \frac{\cos\varphi}{C_l/C_d}\right) r dr \tag{4.23}$$

Eq. (4.23) shows that, to deliver sufficient torque, slender blades (low value of the chord c) require a high value of the combination $V^2{}_1$ (a high design tip−speed ratio) and C_l (a high design lift). Potentially, slender blades can ensure both low extreme and low

fatigue loads, but due to the limited absolute thickness more blade mass may be needed to satisfy all structural requirements.

In addition to the airfoil shape and the required design lift coefficient, the local Reynolds number and the expected degree of blade leading edge contamination also need to be addressed, since failure to establish a trustworthy set of data reflecting blade operating conditions may result in failure to predict both rotor power and rotor loads with sufficient accuracy. As explained earlier, the Reynolds number and the maximum lift–drag ratio for a specific airfoil are closely linked. A first estimate of the Reynolds number for a specific data set can be made by taking the product of the local rotational speed $((r/R)V_{tip})$ and the approximate local chord length c divided by 15×10^{-6}. If the chord length is not known, a rule of thumb is that the Reynolds number will be between $75R \times 10^3$ and $150R \times 10^3$.

Since generally the aim of the design is to achieve low-cost energy, no doubt a number of iterations will be needed in order to find the right balance between aerodynamic efficiency, structural integrity, and sufficiently low blade mass.

4.9.1 Available airfoil data

Unfortunately there still is not much information publicly available on dedicated airfoil designs and their measured performance. Airfoil characteristics have been collected by Bartognioli et al. in a wind turbine airfoil catalog (Bertagnolio et al., 2001). However, the catalog is not complete and basically contains characteristics measured at Reynolds numbers below 3×10^6. For bigger machines, with Reynolds numbers of 3×10^6 or higher and design lift coefficients above unity, Tables 4.2–4.5 summarize what information can be found.

Due to the combination of test Reynolds number and design lift coefficient, a number of airfoils do not appear in the tables. Since 1984, an appreciable number of S8xx airfoils have been designed under the auspices of the National Renewable Energy Laboratory (NREL) in the USA, for wind turbines with various control mechanisms. Information about all of these airfoils can be found via the information portal of NREL's National

Table 4.2 Airfoils suited for wind turbines with a design lift coefficient higher than 1 and publicly available measured characteristics at about Re $= 3 \times 10^6$. Maximum relative thickness of 18%.

Airfoil	t/c	Measured Re	$C_{l,\text{design}}$	$C_{l,\max}$	$(C_l/C_d)_{\max}$	Reference
NACA 63_3–618	0.18	3×10^6	1.1	1.39	138	(Abbott and von Doenhoff, 1959)
NACA 64_3–618	0.18	3×10^6	1.09	1.37	156	(Abbott and von Doenhoff, 1959)
DU 96-W-180	0.18	3×10^6	1.06	1.25	143	(Timmer and van Rooij, 2003)
FX S03–182	0.182	3×10^6	1.04	1.48	157	(Althaus, 1972)

Table 4.3 Airfoils suited for wind turbines with a design lift coefficient higher than 1 and publicly available measured characteristics at about Re = 3×10^6. Maximum relative thickness of 21%.

Airfoil	t/c	Measured Re	$C_{l,\text{design}}$	$C_{l,\max}$	$(C_l/C_d)_{\max}$	Reference
NACA 63_4–421	0.21	3×10^6	1.04	1.33	127	(Abbott and von Doenhoff, 1959)
NACA 64_4–421	0.21	3×10^6	1.04	1.34	142	(Abbott and von Doenhoff, 1959)
DU 93-W-210	0.21	3×10^6	1.22	1.35	141	(Timmer and van Rooij, 2003)
DU 00-W-212	0.212	3×10^6	1.04	1.27	127	(Pires et al., 2016)

Table 4.4 Airfoils suited for wind turbines with a design lift coefficient higher than 1 and publicly available measured characteristics at about Re = 3×10^6. Maximum relative thickness of approximately 25%.

Airfoil	t/c	Measured Re	$C_{l,\text{design}}$	$C_{l,\max}$	$(C_l/C_d)\text{max}$	Reference
DU 91-W2–250	0.25	3×10^6	1.21	1.37	128	(Timmer and van Rooij, 2003)
AH 93-W-257	0.257	3×10^6	1.2	1.41	121	(Althaus, 1984)
NACA 63_{421}–425[a]	0.25	3×10^6	1.07	1.28	120	(Timmer and van Rooij, 2003)
S814	0.241	3×10^6	1.11	1.41	116	(Somers, 1997)

[a]This airfoil has an unsatisfactory rough behavior.

Table 4.5 Airfoils suited for wind turbines with a design lift coefficient higher than 1 and publicly available measured characteristics at about Re = 3×10^6. Maximum relative thickness of more than 25%.

Airfoil	t/c	Measured Re	$C_{l,\text{design}}$	$C_{l,\max}$	$(C_l/C_d)_{\max}$	Reference
DU 97-W-300	0.30	3×10^6	1.39	1.57	98	(Timmer and van Rooij, 2003)
DU 97-W-300Mod	0.30	2.9×10^6	1.34	1.47	108	(Timmer and Schaffarczyk, 2004)
AH 93-W-300	0.30	2.5×10^6	1.02	1.16	66	(Althaus, 1984)
AH 94-W-301	0.301	2.5×10^6	1.33	1.43	100	(Althaus, 1984)
FX 69-274	0.274	3×10^6	1.07	1.31	100	(Althaus, 1984)
FX 77-W-270 S[a]	0.27	3×10^6	1.54	1.94	118	(Althaus, 1984)
FX 77-W-343[a]	0.343	3×10^6	1.72	2.01	96	(Althaus, 1984)
DU 00-W-350[a]	0.35	3×10^6	1.21	1.40	81	(van Rooij and Timmer, 2003)

[a]These airfoils have an unsatisfactory rough behavior without the use of vortex generators

Wind Technology Center. Many designs were verified in the Ohio and Penn State University wind tunnels but, since the designs mainly focused on small to medium size machines (2–50 m diameter), generally containing airfoils with low maximum lift coefficients, here measurements also concentrated on lower Reynolds numbers and airfoil models with design lift coefficients well below one. Of the more recent airfoils that would apply to the bigger machines on the basis of their design lift coefficient, only performance predictions are available.

The development of Risø's A1, B1, C2, and P airfoil families was supported by full-scale tests and extensive measurement campaigns in the Velux wind tunnel in Denmark (Bak et al., 2004). Since the maximum attainable Reynolds number in this wind tunnel is 1.6×10^6, they do not appear in the tables. The coordinates of the Risø airfoils and measurements at higher Reynolds numbers are not publicly available. Moreover, the FFA-W3 series of airfoils (Björk, 1990), although worth considering, are not included in the tables as no measurements of these airfoils at Reynolds numbers higher than 1.6×10^6 (24% and 30% thick in the Velux tunnel) exist in the public domain. It must be noted that the NREL S8xx and the Risø airfoils are subject to license agreements and the use of the airfoils is generally not free of costs.

The appearance of airfoil FX S03−182 in Table 4.2 is to show that occasionally glider airfoils may also come into consideration for this thickness. The references in Tables 4.3 to 4.5 have been chosen to stay close to the original source. In particular the DU-airfoils have been the subject of a number of studies, with experiments in facilities other than the TUDelft wind tunnel. Additional data on these airfoils can be found in e.g., (Bak et al., 2022).

Though many rotor designs put more weight on the structural efficiency at the inner part of the rotor, the aerodynamic efficiency of this part of the rotor must not be ignored. Paying special attention to the aerodynamics of the thickest airfoils may increase the total rotor power by a few percent. Due to the limited aerodynamic performance of thick airfoils, especially in cases of leading edge contamination or erosion, generally vortex generators are applied on the inboard part of the blade to suppress early flow separation, which would adversely impact the local lift and drag performance.

4.9.2 Establishing the data

If data at a Reynolds number of 6×10^6 are needed, a common value for present day machines, from the airfoils listed, only the 18% NACA airfoils (with design lift coefficients of about 1.0 at this Reynolds number), DU 00-W-212, DU 91-W2-250 (Rogowski et al., 2018) and the modified DU airfoil would remain. Data for even higher Reynolds number can only be found for DU 00-W-212, whose characteristics were measured in the European AVATAR project at Reynolds numbers between 3×10^6 and 15×10^6, and the DU97-W-300Mod at Reynolds numbers between 2×10^6 and 10×10^6 (Freudenreich et al., 2004). This already illustrates that measurements of airfoil sections projected for blade design often do not exist in the public domain at the required Reynolds number or even do not exist at all. It is therefore necessary to predict the airfoil performance by computations using either panel codes or CFD codes. The measured performance of the airfoil at a lower Reynolds number or the performance of an aviation airfoil at the required Reynolds number can be used as a check on the validity of the predictions, provided that the measured data come from a trustworthy source.

As an outcome of the simulations, two sets of airfoil characteristics should be established: one set assuming a clean airfoil surface (free transition computations) and one set assuming a contaminated airfoil leading edge. Using XFOIL or RFOIL in the evaluation process the model for free transition, the "*e*-to-the-*n*th" method, requires the

factor n as an input. For very low turbulent flow $n = 9$ or 10 is required, but for many high quality wind tunnels n should have values of 6 or 7.

As described in Section 4.4.1 the degree of blade soiling is generally not known and even if it were known there is a limit to what can be simulated with prediction codes. In XFOIL/RFOIL, transition can be fixed on the leading edge so that the entire surface is turbulent. This, however, is not the same as tripping the boundary layer in an experiment, where the tripping device, in addition to making the boundary layer turbulent, by its own thickness adds to the boundary layer thickness and momentum loss thickness. This is demonstrated in Fig. 4.21, which shows the measured and calculated performance of airfoil NACA 64_3−618 in both the clean and the rough condition. In the predictions, transition was fixed at $x/c = 0.1\%$ on the suction side and $x/c = 10\%$ at the pressure side. The graph clearly shows that the effect of the wrap-around roughness on drag and lift is much more severe than can be calculated by the panel code.

If measurements for a specific airfoil do not exist at the required Reynolds number, they should be corrected for this prior to being used in the design. This can be done by determining the changes in c_l, c_d, and c_m in the computations while going from the Reynolds number of the experiment to the required value for the design. These changes can then be added to the measurements so that two sets of data exist: one set assuming a clean airfoil surface and one set assuming a contaminated airfoil surface, where both sets reflect the correct Reynolds number.

Airfoil characteristics for wind turbine rotor aerodynamic design should to some extent reflect the existence of soiled blades, but on the other hand the rotor design should not be too conservative resulting in the power being too low or loads being too high. The challenge in the blade design process is to ensure that one set of airfoil

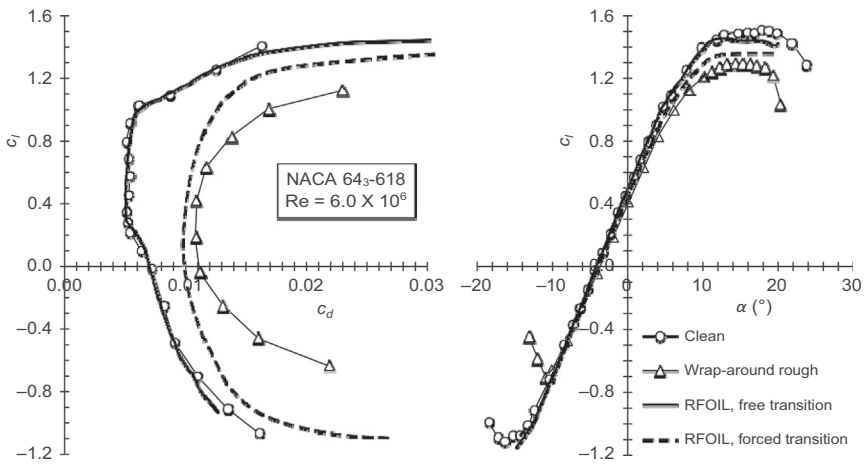

FIGURE 4.21 The measured and predicted performance of airfoil NACA 64_3-618 in the clean and rough condition. RFOIL free transition with $n = 10$. Forced transition at $x/c = 0.1\%$ on the suction side and 10% at the pressure side. In contrast to Fig. 4.3 the predicted drag here is multiplied by a factor of 1.08 to show the good match at the boundaries of the low drag region.

characteristics represents the state of the blade surface during a longer period of time. One way of handling this is to blend clean surface airfoil characteristics with characteristics representing a contaminated leading edge, while adding weight factors to the clean and rough airfoil c_l, c_d, and c_m curves, e.g., 70% for the clean condition and 30% for the soiled blade.

The result of blending data that are based on different surface configurations is inherently two-dimensional because the computations and measurements assume two-dimensionality. However, on a rotating blade the flow is exposed to, e.g., centrifugal forces, Coriolis forces, tip effects, and root effects, resulting in a high degree of three-dimensional flow, especially when separation occurs. As explained earlier in this chapter, models exist to correct for these effects, so the established 2-D data set should be corrected accordingly. Even though some control strategies for wind turbine rotors ensure that separation is not a major factor, it is still important to correct for three-dimensional flow because it is very likely that the flow, especially on the inner part of the rotor, will separate.

4.10 Future trends

The ongoing upscaling of wind turbine blades results in blade section Reynolds numbers of 10×10^6 and more. There still is little experience with these high Reynolds numbers and results from the European AVATAR project have shown that CFD codes as well as panel codes like XFOIL/RFOIL are not yet sufficiently calibrated for these conditions, which creates additional uncertainty in the simulations.

Until a few years ago the aerodynamic performance of thin to medium thick airfoils ($t/c < 30\%$) received the most attention. With the upscaling of blades to 90 m span and more, thicker airfoils ($t/c > 40\%$) are needed to create the required stiffness. The accuracy of performance prediction of thick airfoils is still not very high. Hence, both the design of thicker airfoils and the ability to predict airfoil performance at these thicknesses at high Reynolds numbers will be the subject of future research.

The fact that the degree of contamination of wind turbine rotor blades is not known in detail hinders the design of new airfoils. Roughness sensitivity plays an important role, especially when thicker airfoils are required for the more outboard sections of the blade. To better map the design space for wind turbine airfoils, blade contamination needs to receive more attention. As concluded previously in this chapter, few verification possibilities exist for predictions with measured two-dimensional wind turbine airfoil performance characteristics at high Reynolds numbers. As a result, wind tunnel testing campaigns will likely focus on the measurements for new thick airfoils with and without leading edge roughness at Reynolds number between 6×10^6 and 15×10^6. One of the major concerns is blade erosion. Erosion and the resulting degradation of turbine performance will remain to be important research topics. Leading edge protection measures and their impact on the blade aerpodynamic characteristics need to be further addressed as well.

New concepts are also likely to be introduced, including static add-ons such as slats and flaps, which generally enhance the lift performance and are particularly good at stabilizing the flow over thick airfoils. Specialized tools are needed to model the performance of such add-ons. Moreover, the use of active devices, such as adaptive trailing edge flaps, micro tabs, dielectric barrier discharge (DBD) plasma actuators and synthetic jets, creates challenges for experiments and predictions because the inherent unsteadiness is not something which can be ignored in the testing and simulation process.

Appendix: Nomenclature

Symbol	Unit	Description
a	—	Induced axial velocity normal to rotor plane
a'	—	Induced tangential velocity in rotor plane
B	—	Number of blades on rotor
c	m	Chord length, distance from leading edge to trailing edge of airfoil
c_d	—	Drag coefficient
^{c}d,max	—	Drag coefficient at 90 degrees or 270 degrees angle of attack
c_l	—	Lift coefficient
$c_{l,\text{design}}$	—	Lift coefficient at which $(c_l/c_d)_{\max}$ is obtained (design lift)
$c_{l,\max}$	—	Maximum lift coefficient
c_l/c_d	—	Lift—drag ratio of airfoil section
$(c_l/c_d)_{\max}$	—	Maximum lift—drag ratio for airfoil section
D	N	Drag on airfoil
F_n	N	Force on airfoil normal to the rotor plane
F_t	N	Tangential force on airfoil in the rotor plane
L	N	Lift on airfoil
r	m	Radial position on rotor blade
Re	—	Reynolds number
U	m/s	Wind speed
V_{rel}	m/s	Relative flow velocity on the airfoil, which is the combination of the axial and the tangential inflow
α	degree	Angle of attack
$^{\alpha}$design	degree	Angle of attack at which $c_{l,design}$ is obtained
φ	degree	Angle between the relative inflow vector and the rotor plane
Ω	rad/s	Rotational speed of the rotor
μ	kg/ms	Air dynamic viscosity
ν	m^2/s	Air kinematic viscosity
ρ	kg/m^3	Air density
θ	degree	Pitch angle
ζ	degree	Trailing edge angle

References

Abbott, I.H., von Doenhoff, A.E., 1959. Theory of Wing Sections. Dover Publications Inc., New York.

Althaus, D., 1972. Stuttgarter Profilkatalog I. Stuttgart University, Germany.

Althaus, D., 1984. Niedriggeschwindigkeitsprofile − Airfoils and Experimental Results from the Laminar Wind Tunnel of the Institute for Aerodynamics and Gas Dynamics of the Stuttgart University, Stuttgart, Germany, ISBN 3-528-03820-9.

Anderson, J.D., 2011. Fundamentals of Aerodynamics, fifth ed. McGraw- Hill, New York.

ANSYS CFX, www.ansys.com.

ANSYS Fluent, www.ansys.com.

Bak, C., 2004. 'Udledning af profildata' (in Danish). In: Bak, C. (Ed.), Risø-R-1434(DA), *Research in Aero-Elasticity*. Risø National Laboratory, Roskilde, Denmark.

Bak, C., Fuglsang, P., Gaunaa, M., Antoniou, I., April 2004. Design and verification of the Risø-P airfoil family for wind turbines. In: Proceedings of the Conference the Science of Making Torque from Wind, Delft, the Netherlands, pp. 16−24.

Bak, C., Johansen, J., Andersen, P.B., 2006. Three-dimensional corrections of airfoil characteristics based on pressure distributions. In: Proc. European Wind Energy Conference & Exhibition (EWEC), Athens, Greece.

Bak, C., Andersen, P.B., Madsen, H.A., Gaunaa, M., Fuglsang, P., Bove, S., August 18−21, 2008. Design and verification of airfoils resistant to surface contamination and turbulence intensity. In: AIAA 2008−7050; 26th AIAA Applied Aerodynamics Conference, Honolulu, Hawaii.

Bak, C., Madsen, A.H., Fuglsang, P., Rasmussen, F., 1999. Observations and hypothesis of double stall. Wind Energy 2, 195−210.

Bak, C., Olsen, A., Fischer, A., Lylloff, O., Mikkelsen, R., Gaunaa, M., Beckerlee, J., Ildvedsen, S., Vronsky, T., Grasso, F., Loeven, A., Broersma, L., Akay, B., Madsen, J., Hansen, R., Kommer, R., 2022. Wind tunnel benchmark tests of airfoils. J. Phys. Conf. Ser.2265 (022097). https://doi.org/10.1088/1742-6596/2265/2/022097.

Barone, M.F., Berg, D., January 2009. Aerodynamic and aero-acoustic properties of a flat- back airfoil: an update. In: AIAA 2009−271.

Bertagnolio, F., Sørensen, N., Johansen, J., Fuglsang, P., August 2001. Wind Turbine Airfoil Catalogue, Risø-R-1280(EN). Risø National Laboratory, Roskilde, Denmark, ISBN 8755029108.

Björk, A., 1990. Coordinates and Calculations for the FFA-W1-xxx, FFA-W2-xxx and FFA-W3-xxx Series of Airfoils for Horizontal axis Wind Turbines. FFA TN 1990−15, FFA, Stockholm, Sweden.

Boorsma, K., et al., 2015. New airfoils for high rotational speed wind turbines. In: Madsen, H.A. (Ed.), InnWind.eu, Deliverable 2.12. DTU Wind, Denmark.

Caboni, M., Minisci, E., Riccardi, A., 2018. Aerodynamic design optimization of wind turbine airfoils under aleatory and epistemic uncertainty. J. Phys. Conf. Ser. 1037 (042011). https://doi.org/10.1088/1742-6596/ 1037/4/042011.

Chaviaropoulos, P.K., Hansen, M.O.L., June 2000. Investigating three-dimensional and rotational effects on wind turbine blades by means of a quasi-3D Navier Stokes solver. J. Fluid Eng. 122, 330−336.

van Dam, C., Mayda, E., Chao, D., Jackson, K., Zuteck, M., Berry, D., 2005. Innovative structural and aerodynamic design approaches for large wind turbine blades. In: AIAA Paper 2005−0973.

Cheng, J., Zhu, W.J., Fischer, A., Garcia, N.R., Madsen, J., Chen, J., Shen, W.Z., 2014. Design and validation of the high performance and low noise CQU-DTU-LN1 airfoils. Wind Energy 17 (12), 1817−1833.

Drela, M., June 1989. XFOIL: an analysis and design system for low Reynolds number air- foils. In: Conference on Low Reynolds Number Airfoil Aerodynamics, University of Notre Dame.

Du, Z., Selig, M.S., January 12–15, 1998. A 3-D stall-delay model for horizontal axis wind tur- bine performance prediction. In: AIAA-98–0021, 36th AIAA Aerospace Sciences Meeting and Exhibit, 1998 ASME Wind Energy Symposium, Reno, NV, USA.

Ferziger, J.H., Peric, M., 2001. Computational Methods for Fluid Dynamics, 3rd Revised Edition. Springer, December, ISBN 3540420746.

http://bladecleaning.com. (Accessed 16 August 2022).

Freudenreich, K., Kaiser, K., Schaffarczyk, A., Winkler, H., Stahl, B., 2004. Reynolds number and roughness effects on thick airfoils for wind turbines. Wind Eng. 28 (5), 529–546.

Fuglsang, P., Bak, C., 2004. Development of the Risø wind turbine airfoils. Wind Energy 7, 145–162.

Gault, D.E., 1957. A Correlation of Low-Speed, Airfoil-Section Stalling Characteristics with Reynolds Number and Airfoil Geometry. Tech. Note 3963. NACA, USA.

Grasso, F., 2014. Airfoils for Large Offshore Wind Turbines: Design and Wind Tunnel Testing. In: EWEA 2014, Barcelona.

Hand, M.M., Simms, D.A., Fingersh, L.J., Jager, D.W., Cotrell, J.R., Schreck, S., Larwood, S.M., December 2001. Unsteady Aerodynamics Experiment Phase VI: Wind Tunnel Test Configurations and Available Data Campaigns. NREL/TP-500–29955, National Renewable Energy Laboratory, Golden, Colorado, USA.

Hansen, T.H., 2018. Airfoil optimization for wind turbine application. Wind Energy 21, 502–514. https://doi.org/10.1002/we.2174.

Hoerner, S.F., 1965. Fluid-dynamic Drag. Published by the author.

Zahle, F., Bak, C., Soerensen, N.N., Vronsky, T., Gausern, N., 2014. Design of the LRP airfoil series using 2D CFD. J. Phys. Conf. Ser. 524 (012020). https://doi.org/10.1088/1742-6596/524/1/012020.

Johansen, J., Sørensen, N.N., Mikkelsen, R., 2004. 'Rotoraerodynamic', (in Danish). In: Bak, C. (Ed.), Risø-R-1434(DA), Research in Aeroelasticity. Risø National Laboratory, Roskilde, Denmark.

Lindenburg, C., July, 2003. Investigation into rotor blade aerodynamics. Report ECN— 03–25.

Lindenburg, C., November 22–25, 2004. Modelling of rotational augmentation based on engineering considerations and measurements. In: Proc. European Wind Energy Conference, London.

Llorente, E., Ragni, D., 2020. Trailing-edge serrations effect on the performance of a wind turbine. Renew. Energy. 147, 437–446. https://doi.org/10.1016/j.renene.2019.08.128.

Lutz, T., Wuertz, W., Herrig, A., Braun, K., Wagner, S., 2004. Numerical optimization of silent airfoil sections. In: Institut für Aerodynamik und Gasdynamik (IAG). Universität Stuttgart, Stuttgart.

Madsen, H.A., Rasmussen, F., 1988. Derivation of three-dimensional airfoil data on the basis of experiment and theory. In: Proceedings of the AWEA Windpower Conference, Honolulu, HI, USA, 88.

McGhee, R.J., Beasley, W.D., 1973. Low-speed Aerodynamic Characteristics of a 17-Percent-Thick Airfoil Section Designed for General Aviation Applications. NASA TN D-7428.

Mendez, B., Mundiate, X., SanMiguel, U., 2014. Airfoil family design for large offshore wind turbine blades. J. Phys. Conf. Ser. 524 (012022). https://doi.org/10.1088/1742-6596/524/1/012022.

Menter, F.R., August 1994. Two-equation eddy-viscosity turbulence models for engineering Applications. AIAA J. 32 (8), 1598–1605.

Michelsen, J.A., 1992. Basis3d – a Platform for Development of Multiblock PDE Solvers. Technical Report afm 92–05, Technical University of Denmark.

Michelsen, J.A., 1994. Block Structured Multigrid Solution of 2D and 3D Elliptic PDE's'. Technical report afm 94–06, Technical University of Denmark.

OpenFOAM, www.openfoam.com.

van Rooij, R.P.J.O.M., September 1996. 'Modification of the Boundary Layer in XFOIL for Improved Airfoil Stall Prediction'. Report IW-96087R. Delft University of Technology, Delft, The Netherlands.

Sørensen, N.N., June 1995. 'General purpose flow solver applied to flow over hills'. Risø-r- 827(en). Risø National Laboratory, Denmark.

Mishnaevsky Jr, l., Hasager, C.B., Bak, C., Tilg, A-M., Bech, J.I., Doagou, R.S., Fæster, S., 2021. Leading edge erosion of wind turbine blades: understanding, prevention and protection. Renew. Energy 169, 963–969. https://doi.org/10.1016/j.renene.2021.01.044.

Pires, O., Mundiate, M., Ceyhan, O., Snel, H., 2016. Analysis of high Reynolds numbers effects on a wind turbine airfoil using 2D wind tunnel test data. J. Phys. Conf. Ser. 753. https://doi.org/10.1088/1742-6596/753/2/022047.

Rogowski, K., Hansen, M., Hansen, R., Piechna, J., Lichota, P., 2018. Detached Eddy simulation Model for the DU-91-W2-250 Airfoil. J. Phys. Conf. Ser. 1037. https://doi.org/10.1088/1742-6596/1037/2/022019.

Skrzypiński, W., February 2012. 'Analysis and Modeling of Unsteady Aerodynamics with Application to Wind Turbine Blade Vibration at Standstill Conditions' (Ph.D. thesis). DTU Wind Energy.

Snel, H., Houwink, R., van Bussel, G.J.W., Bruining, A., 1993. Sectional prediction of 3D effects for stalled flow on rotating blades and comparison with measurements. In: Proc. European Community Wind Energy Conference, Lübeck-Travemünde, Germany, 8–12 March. H.S. Stephens & Associates, pp. 395–399.

Somers, D.M., 1997. Design and Experimental Results for the S814 Airfoil. Report NREL/SR-440–6919.

Spera, A.D., June 2010. Models of Lift and Drag Coefficients of Stalled and Unstalled Airfoils in Wind Turbines and Wind Tunnels. NASA/CR—2008–215434.

STAR-CD. http://www.cd-adapco.com.

Tangler, J., Kocurek, J.D., January10–13, 2005. Wind turbine post-stall airfoil performance characteristics guidelines for blade-element momentum methods. In: 43rd AIAA Aerospace Sciences Meeting and Exhibit. Reno, Nevada.

Tangler, J.L., Somers, D.M., 1995. 'NREL Airfoil Families for Hawt's' Proc. WINDPOWER'95, Washington D.C, pp. 117–123.

Timmer, W.A., 2009. An overview of NACA 6-digit airfoil series characteristics with reference to airfoils for large wind turbine blades. In: AIAA-2009–0268, 47th AIAA Aerospace Sciences Meeting Including the New Horizons Forum and Aerospace Exposition 5–8 January 2009, Orlando, Florida, USA.

Timmer, W.A., 2020. A simple method to estimate the airfoil maximum drag coefficient. J. Phys.: Conf. Ser 1618 (052068).

Timmer, W.A., June 28–30, 2010. Aerodynamic characteristics of wind turbine blade airfoils at high angles of attack. In: Conference Proceedings Torque 2010, the Science of Making Torque from Wind. Heraklion, Greece, pp. 71–97.

Timmer, W.A., Bussel, G.J.W. van, 2007. Wind turbine airfoil design and testing. In: Wind Turbine Aerodynamics: A State-of-the Art. von Karman Institute for Fluid Dynamics, Brussels. VKI LS 2007-5.

Timmer, W.A., Schaffarczyk, A.P., 2004. The effect of roughness at high Reynolds numbers on the performance of aerofoil DU 97-W-300Mod. Wind Energy 7 (4), 295–307. https://doi.org/10.1002/we.136.

Timmer, W.A., van Rooij, R.P.J.O.M., January 2003. Summary of the Delft University wind turbine dedicated airfoils. In: 41st Aerospace Sciences Meeting, Paper No. AIAA- 2003–0352, Reno, USA.

van Rooij, R.P.J.O.M., Timmer, W.A., January 2003. Roughness Sensitivity Considerations for Thick Rotor Blade Airfoils. In: 41st Aerospace Sciences Meeting, Paper no. AIAA- 2003–0350, Reno, USA.

Viterna, L.A., Corrigan, R.D., July 1981. Fixed Pitch Rotor Performance of Large Horizon- Tal axis Wind Turbines. DOE/NASA Workshop on Large Horizontal Axis Wind Turbines, Cleveland, Ohio.